Journal of Materials Research and Technology 39 (2025) 715–729

Contents lists available at ScienceDirect

Journal of Materials Research and Technology

journal homepage: www.elsevier.com/locate/jmrt

Microstructure and mechanical properties of microwave-sintered Ni-alloyed Ti_3SiC_2/graphene co-reinforced lamellar porous Fe-7.5Cu composites

Ailun Deng [a,b], Rui Shu [a,b,*], Hongliang Sun [a,b], Zixuan Wu [c], Liu Yang [d], David Hui [e], Xiaosong Jiang [a,b,**]

[a] School of Materials Science and Engineering, Southwest Jiaotong University, Chengdu, Sichuan, 610031, China
[b] Key Laboratory of Advanced Technologies of Materials, Ministry of Education, Chengdu, 610031, China
[c] School of Engineering and Materials Science, Queen Mary University of London, London, E1 4NS, United Kingdom
[d] Institute for Applied Materials (IAM-WK), Karlsruhe Institute of Technology (KIT), Karlsruhe, 76131, Germany
[e] Department of Mechanical Engineering, University of New Orleans, New Orleans, LA, 70148, USA

ARTICLE INFO

Keywords:
Flake powder metallurgy
Microwave sintering
Ni alloying
Microstructure
Mechanical properties

ABSTRACT

Porous Fe–Cu alloys are crucial for frictional applications such as bearings and gears, where their low density and porosity are advantageous for lubrication. However, the inherent microstructural defects hinder the achievement of high strength and ductility under harsh conditions, limiting their durability and widespread application. This study aims to address this deficiency through the synergistic optimization of Ni alloying and dual-phase reinforcements within biomimetic layered structures. The method combines microwave sintering with flake powder metallurgy technology, incorporating 1–7 % Ni into the Fe–7.5Cu matrix, while adding 1 % copper-coated graphene (GNP(Cu)) and 6 % Ti_3SiC_2 to enhance the control effects. The composite material with 7 % Ni demonstrates excellent performance: a tensile strength increase of 25.13 %, reaching 232.3 MPa, and a compressive strength increase of 16.14 %, reaching 675.1 MPa, with an average copper particle size increase of 79.46 % due to the sintering effects promoted by Ni. These improvements arise from the solid-solution effect and grain refinement induced by nickel, complemented by the Orowan effect, thermal mismatch, and load transfer mechanisms from GNP(Cu), Ti_3SiC_2, and TiC/Fe_3C products, which together suppress dislocations and refine the microstructure while maintaining approximately 23 % porosity. The advantage of this approach lies in achieving a balanced synergy between strength and ductility, avoiding excessive densification, and providing new insights into the alloying strategies for high-performance sustainable porous metal matrix composites in harsh industrial environments.

1. Introduction

Porous Fe–Cu alloys, with their low density, high specific surface area, and flexible porosity control, exhibit significant potential in frictional applications such as bearings, gears, and sliding components. These areas demand strict standards for low friction and high wear resistance, where the Fe matrix ensures structural rigidity and load-bearing capacity, while Cu alloying enhances corrosion resistance and thermal conductivity [1]. However, the porous nature often leads to a notable reduction in strength due to limited particle-to-particle contact and crack propagation under cyclic stress, which restricts their durability in harsh environments [2,3]. To address these shortcomings, alloying optimization of porous Fe–Cu alloys has become a research focus. While elements like Cr, Mo, or Mn can be considered, they have significant limitations: Cr can improve wear resistance and hardness but tends to embrittle the material and form unstable oxides during sintering, reducing toughness [4]. Mo enhances high-temperature strength and creep resistance; however, its high cost and limited solubility restrict its economic viability and uniform distribution [5]. Mn, though beneficial for quenching ability and cost reduction, can lead to phase separation and increased porosity during high-temperature sintering, further hindering densification due to its susceptibility to oxidation [6].

* Corresponding author. School of Materials Science and Engineering, Southwest Jiaotong University, Chengdu, Sichuan, 610031, China.
** Corresponding author. Key Laboratory of Advanced Technologies of Materials, Ministry of Education, Chengdu, 610031, China.
E-mail addresses: r.shu@swjtu.edu.cn (R. Shu), xsjiang@swjtu.edu.cn (X. Jiang).

https://doi.org/10.1016/j.jmrt.2025.09.185
Received 17 August 2025; Received in revised form 8 September 2025; Accepted 20 September 2025
Available online 20 September 2025

Therefore, the introduction of Ni as a preferred alloying element is crucial. Ni, by solid solution in the Fe–Cu matrix, induces lattice distortion, thereby increasing hardness and yield strength [7]. Additionally, Ni improves the diffusion dynamics of Cu, suppresses sintering expansion, promotes densification, and reduces residual porosity [8]. In the enhancement of reinforcing phases, Ti_3SiC_2 with a MAX structure and graphene nanoplatelets (GNP) serve as key reinforcements: Ti_3SiC_2's layered crystals combine ceramic rigidity and metallic plasticity, promoting heterogeneous nucleation and grain refinement [9]. GNP's two-dimensional carbon framework provides high modulus, supporting stress dispersion and crack blockage [10]. The interaction between Ni, Ti_3SiC_2, and GNP further stabilizes the phase boundary and refines the microstructure, potentially achieving a comprehensive performance improvement.

To address the strength limitations of porous Fe–Cu alloys, researchers have drawn inspiration from the toughening mechanisms found in biological materials such as seashells. A bioinspired laminated structure-resembling a "brick-and-mortar" architecture-has been developed. In this design, hard "bricks" (mineral layers) are alternated with soft "mortar" (buffer phases) to achieve a balance between strength and ductility. The mortar layers not only provide structural stiffness but also accommodate deformation, allowing the rigid bricks to undergo slight displacements to relieve stress concentrations. The bricks primarily bear external loads [11]. This layered architecture effectively deflects crack propagation, mitigates local shrinkage, and homogenizes the stress distribution, thereby efficiently dissipating fracture energy and enhancing the overall mechanical performance of the structure [12]. Through uniform dispersion of reinforcing phases, this bioinspired strategy has successfully refined the microstructure of micron-scale metal matrix composites (MMCs), yielding superior strength and ductility compared to conventional MMCs. Graphene nanoplatelets (GNPs), derived from graphite, offer a large surface area and a unique combination of flexibility and stiffness, enabling excellent energy dissipation capabilities. Challenges associated with their dispersion can be overcome using electroless copper plating techniques [13]. Ti_3SiC_2, with its dual ceramic–metallic nature, serves a mortar-like function by combining high hardness with ductility. The addition of Ni further enhances interfacial bonding and promotes the formation of Cu–Ni solid solution phases, leading to improved load transfer efficiency and fracture resistance [14].

To achieve precise control over the porosity of laminated metal matrix composites, advanced powder metallurgy techniques are essential. Conventional methods such as hot pressing (HP) [15]and spark plasma sintering (SPS) [16]have proven effective; however, they often result in over-densification or thermal non-uniformity, which limits their suitability for fabricating porous structures. Although cutting-edge approaches like 3D printing enable excellent compositional and morphological uniformity, they suffer from low fabrication efficiency [17]. Microwave sintering has emerged as a promising solution for achieving high porosity while maintaining a uniform thermal field. As an innovative technique for the rapid processing of ceramics, metals, and composites, it has been successfully applied in the fabrication of medical porous alloys [18]. Unlike traditional heating methods, microwave sintering relies on volumetric interaction between the green compact and electromagnetic waves, converting electromagnetic energy into heat until the sintering temperature is reached, enabling densification and metallurgical bonding. The unique features of microwave sintering-volumetric heating, shortened processing cycles, lower thermal thresholds, and enhanced diffusion kinetics-contribute to microstructural refinement, grain size reduction, and controlled formation of secondary phases [19–21]. These advantages make microwave sintering a powerful tool for tailoring the microstructure and porosity of advanced laminated composites.

Despite progress in alloying and reinforcement strategies for porous Fe–Cu alloys, a critical knowledge gap remains in achieving both high strength and high ductility under harsh conditions, particularly through the synergistic integration of Ni alloying and dual-phase reinforcements within biomimetic layered structures using microwave sintering technology. Conventional approaches often lead to excessive embrittlement caused by ceramic additives or insufficient densification in traditional sintering, thereby limiting their application in frictional components. This study innovatively combines flake powder metallurgy with microwave sintering to fabricate layered porous Fe–7.5Cu composites reinforced synergistically with Ni alloying, Ti_3SiC_2, and graphene. This method enables simultaneous microstructural control and performance optimization. While maintaining controllable porosity, it offers new insights into multiple strengthening mechanisms—including solid-solution strengthening, the Orowan effect, thermal mismatch, and load transfer—thus filling a gap in the field of sustainable, high-performance porous metal matrix composites. Similar principles can be drawn from recent studies on cement-based composites, where nanosilica, fly ash, and pozzolanic materials act synergistically through hydration optimization and interfacial zone strengthening, significantly enhancing fracture toughness, crack resistance, and microstructural integrity [22–26].

2. Experiment

2.1. Raw materials

Porous laminated composites of Fe-7.5Cu-xNi-1.0GNP(Cu)–6Ti_3SiC_2 (x = 1, 3, 5, 7 wt%) were synthesized with varying Ni content. The reinforcement content of 1.0 wt% GNP(Cu) and 6 wt% Ti_3SiC_2 was selected based on prior research into the Fe-7.5Cu porous system, to balance the enhancement of mechanical properties.The starting materials included flake-shaped Fe powder (99.9 %, 400 mesh), flake-shaped Cu powder (99.9 %, 300 mesh), spherical Ni powder (99 %, 1 μm), and Ti_3SiC_2 powder (99.5 %, 250 mesh). Graphene nanoplatelets (GNPs) were modified via an ultrasonic-assisted electroless copper plating method. This process involved surface roughening, sensitization, activation, and chemical deposition steps to produce Cu-coated graphene nanoplatelets (GNP(Cu), 99 %).

2.2. Composites preparation

As shown in Fig. 1, the powders of flake-shaped Fe (7.5 wt%), flake-shaped Cu, spherical Ni, Ti_3SiC_2, and GNP(Cu) were weighed according to the mass ratio of Fe-7.5Cu-xNi-1.0GNP(Cu)–6Ti_3SiC_2 (x = 1, 3, 5, 7 wt %) for the experiment. Under the condition of using tert-butanol as the ball milling medium, the powder mixture was ball-milled in an agate jar at a speed of 300 r/min for 2 h to ensure uniform mixing. The mixture was then transferred to a freeze-drying unit and freeze-dried at −50 °C under vacuum for 24 h to remove the organic solvent. The dried composite powder was then placed into a mold with a diameter of 35 mm and uniaxially pressed at 600 MPa for 1 min to form green bodies, with a thickness of approximately 10 mm (Φ35 mm × 10 mm). The green body was placed in a fiber cotton-insulated furnace and heated in a 2.45 GHz, 5.6 kW microwave sintering furnace (Model HY-ZK6016, Hunan Huazhi Microwave Technology Co., Ltd.). The temperature was ramped at a rate of 40 °C/min to 1100 °C, where it was held for 10 min before being naturally cooled to room temperature. The final Fe-7.5Cu-xNi-1.0GNP (Cu)–6Ti_3SiC_2 (x = 1, 3, 5, 7 wt%) alloy material was obtained.

2.3. Characterization and test

The surface morphology and fracture characteristics of the powders and samples were characterized using a ZEISS Sigma 300 scanning electron microscope (SEM), a Rigaku Ultima IV X-ray diffractometer (XRD), and a FEI Talos F200X transmission electron microscope (TEM). To further investigate the microstructure and composition, selected area electron diffraction (SAED) patterns and energy-dispersive spectroscopy (EDS) data were also collected. The overall density and porosity of the

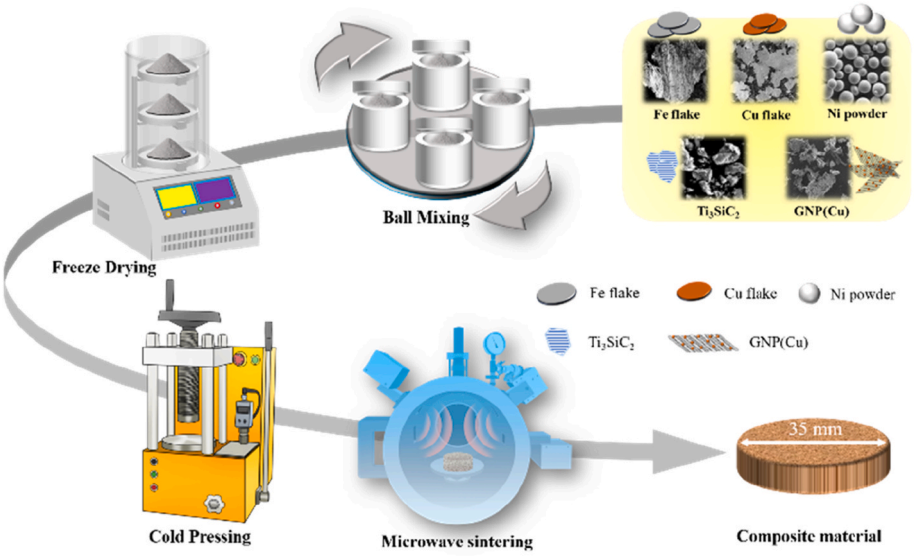

Fig. 1. Preparation process of Fe-7.5Cu-xNi-1.0GNP(Cu)–6Ti_3SiC_2 composite material.

porous Fe-7.5Cu-1.0GNP(Cu)-xTi_3SiC_2 alloys were determined according to ASTM B962-08 standards using the Archimedes water displacement method. Hardness testing was conducted using an HXD-100TM/LCD microhardness tester with a load of 1 kg and a dwell time of 15 s. For mechanical property evaluation, tensile and compression tests were carried out at room temperature using a WDW 3100 universal material testing machine, equipped with a CBY1 10/2.5 extensometer, at a loading rate of 0.5 mm/min. The tensile samples were standard-sized rectangular bars (33 × 9.5 × 2 mm), and the compression samples were rectangular blocks (5 × 5 × 10 mm). Each test was repeated three times, and the standard deviation of the tensile and compression strengths was maintained within 5 MPa to ensure the reproducibility and reliability of the data.

3. Results and discussion

3.1. Microscopic morphology of various powders

As shown in Fig. 2(a), the GNPs exhibit a layered, sheet-like morphology, with their surfaces largely covered by a uniform copper (Cu) coating, indicating the effectiveness of the Cu plating process. A small portion of the GNP edges remain exposed due to incomplete coverage, with delamination defects accounting for approximately 3.13 % of the total surface area, and the largest defect region measuring less than 5 μm. These exposed areas may adversely affect the interfacial bonding strength between GNPs and the Fe matrix during sintering. As a carbon-based reinforcing phase, the Cu coating on GNPs not only reduces the extent of reaction with the Fe matrix but also enhances interfacial compatibility. This promotes more efficient load transfer and dispersion strengthening, which is crucial for improving the mechanical performance of the composites [27].

As shown in Fig. 2(b), the morphology of the composite powders after ball milling is presented. Under milling conditions of 300 r/min for 2 h, the flake-shaped Fe and Cu powders underwent significant flattening and cold welding, resulting in refined morphology, reduced particle size, and a narrower size distribution. The brittle Ti_3SiC_2 particles were fractured into submicron-scale fragments, improving their dispersibility within the matrix. GNPs exhibited good orientation and dispersion, likely due to the improved wettability imparted by the Cu coating. The Ni powder contributed to solid solution strengthening or acted as a secondary phase, influencing both powder homogeneity and subsequent sintering behavior. Furthermore, as shown in Fig. 2(c), the morphological compatibility between the flake-like GNP(Cu) nanoparticles and the flake-shaped matrix powders increased the contact area, promoting preferential parallel stacking during ball milling and cold pressing. This enhanced dispersion uniformity and laid the foundation for constructing the layered composite structure.

3.2. Phase composition and microstructure of Fe-7.5Cu-xNi-1.0GNP (Cu)–6Ti_3SiC_2 composite

3.2.1. XRD

As shown in the diffraction patterns of the Fe-7.5Cu-xNi-1.0GNP (Cu)–6Ti_3SiC_2 composites in Fig. 3(a), all four samples with varying Ni contents (x = 1, 3, 5, 7 wt%) exhibit similar phase compositions. The primary phases include the characteristic peaks of α-Fe (110), (200), (211), Cu (111), (200), (220), and Ti_3SiC_2 (100), (105). Additionally, TiC peaks (111), (220) are detected, originating from the partial decomposition of Ti_3SiC_2 during high-temperature microwave sintering. This decomposition behavior is attributed to the thermal instability of

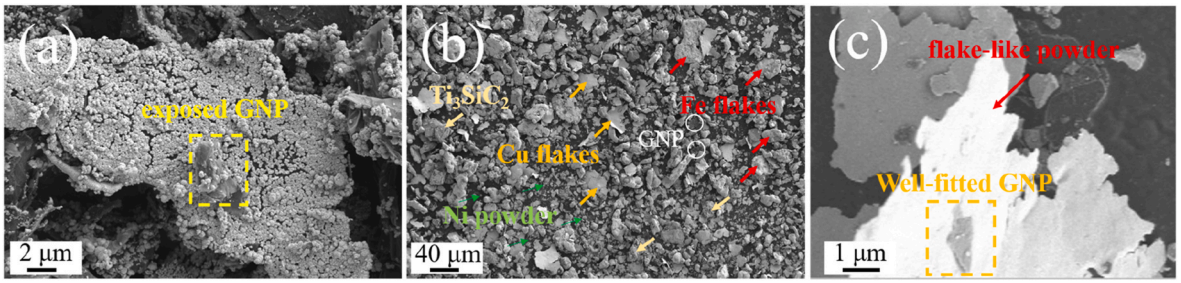

Fig. 2. (a) Morphology of GNP(Cu), (b) morphology of composite powder.(c) GNP adheres well to flake-like powders.

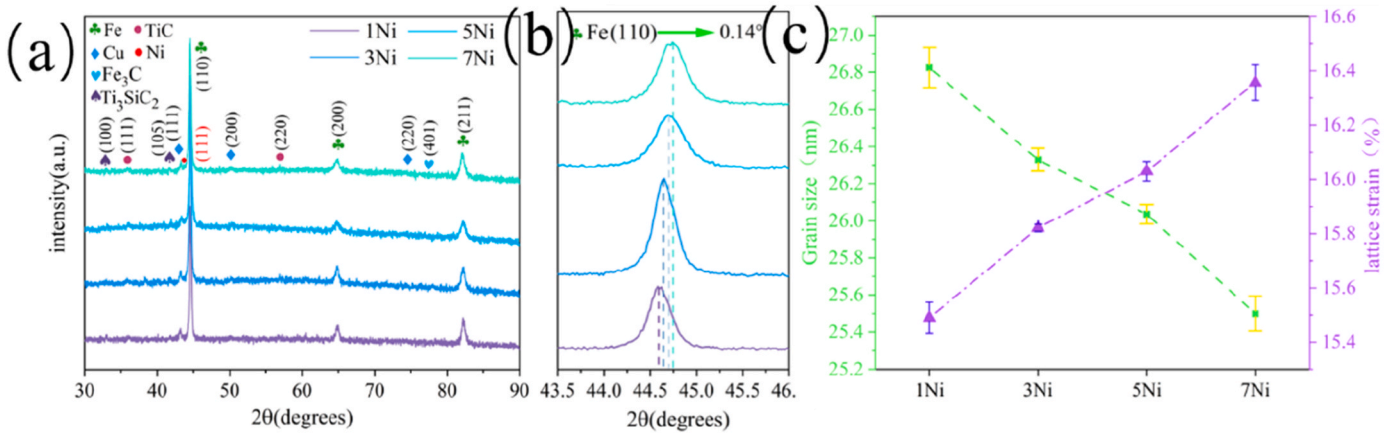

Fig. 3. (a) XRD patterns of samples with different Ni contents, (b) magnified view of the Fe(110) peak, (c) average grain size and lattice distortion.

the MAX-phase Ti_3SiC_2, which undergoes rapid de-siliconization under fast heating, leading to the formation of TiC and SiC. However, the SiC peaks are not clearly observable, likely due to their low intensity or overlap with other peaks [28]. No distinct Ni diffraction peaks are observed in samples with low Ni content, suggesting that Ni atoms primarily dissolve into the Fe–Cu matrix, forming Fe–Ni or Cu–Ni solid solutions. In contrast, the 7 wt% Ni sample exhibits a noticeable Ni (111) peak, indicating the precipitation of Ni due to solubility saturation. This behavior aligns with the limited solid solubility of Ni in Fe and its complete miscibility with Cu. At higher concentrations, excess Ni may precipitate as a secondary phase, potentially affecting the phase stability of the composite. As shown in the magnified view in Fig. 3(b), the Fe (110) peak shifts to higher 2θ angles with increasing Ni content, with an observed offset of approximately 0.14°. This shift reflects a reduction in lattice parameter, primarily caused by the substitution of Fe atoms (atomic radius = 0.126 nm) with smaller Ni atoms (atomic radius = 0.124 nm), resulting in lattice contraction and induced lattice strain. This trend follows Vegard's law, which describes the compositional dependence of lattice constants in solid solutions. In powder metallurgy-based Fe–Ni alloys, such peak shifts can be used to evaluate the degree of alloying and are beneficial for enhancing mechanical properties [29]. The effect of Ni content on the average crystallite size of the Fe phase can be quantitatively estimated using the Debye–Scherrer equation [30]:

$$D = \frac{K\lambda}{\beta \cos\theta} \tag{1}$$

where D is the crystallite size (nm), K is the Scherrer constant (~0.89), λ is the X-ray wavelength (~0.154 nm), β is the full width at half maximum (FWHM) in radians, and θ is the diffraction angle. Calculations reveal that as Ni content increases, the crystallite size of the Fe phase decreases from 26.83 nm (x = 1 wt%) to 25.47 nm (x = 7 wt%). This reduction indicates that Ni, as an alloying element, promotes solid-solution strengthening and pins grain boundaries, inhibiting grain growth and enhancing refinement. This observation aligns with the Hall-Petch relationship, which correlates smaller grain sizes with increased yield strength. Additionally, a strong correlation exists between lattice strain and crystallite size in metallic materials, as determined by the following equation [30]:

$$\varepsilon = \frac{D}{4\tan\theta} \tag{2}$$

As Ni content increases, lattice strain also rises, exhibiting an inverse relationship with crystallite size. This behavior stems from lattice distortions and residual stress induced by Ni addition. Such strain-induced strengthening enhances dislocation interactions at the nanoscale, thereby improving the material's hardness and wear resistance. However, excessive lattice strain may pose a risk of embrittlement. Overall, the gradient regulation of Ni content effectively optimizes the composite's microstructure. Through peak shifts induced by solid solution formation, grain refinement, and increased lattice strain, a robust structural foundation is established for enhanced mechanical performance. The corresponding variations in crystallite size and lattice distortion are illustrated in Fig. 3(c).

3.2.2. SEM surface topography analysis

The surface morphology of the Fe-7.5Cu-1.0Ni-1.0GNP(Cu)–6Ti_3SiC_2 composite, observed under SEM in backscattered electron (BSE) mode (Fig. 4(a)), reveals a complex multiphase microstructure with distinct defect features. The Fe matrix, indicated by red arrows, appears as a light gray phase and serves as the primary load-bearing framework. In contrast, the Cu phase, highlighted by light blue circles, exhibits a brighter contrast and is mainly enriched along grain boundaries and pore peripheries. This distribution is attributed to Cu's lower melting point and rapid diffusion driven by selective microwave heating. Coupled with the nanoscale reinforcement of GNPs, Cu tends to migrate into powder interstices, effectively filling voids [31]. Cavity-like pores, marked by white arrows, display rounded morphologies. Their formation is primarily due to the high heating rate and short sintering time inherent to microwave sintering, which limit the diffusion and bonding of flake-shaped Fe and Cu powders, thereby preserving some of the initial voids from cold pressing. The presence of these pores is essential to the material's intended porous architecture. Fissure-like pores, shown by blue arrows, appear as linear cracks, likely resulting from residual tensile stresses caused by thermal mismatch between the Ti_3SiC_2 reinforcement and the Fe matrix during furnace cooling. Additionally, the fragmentation of brittle Ti_3SiC_2 particles during ball milling and the stress concentration induced by the layered GNP structure may contribute to crack propagation [32]. Ti_3SiC_2 particles, indicated by yellow arrows, are distributed within the size range of 10–30 μm and exhibit good interfacial bonding with the matrix, without significant voids. This suggests that microwave heating enhances the wettability and chemical bonding between Ti_3SiC_2 and Fe. The magnified view in Fig. 4(b) and the corresponding EDS line scan along the yellow path (Fig. 4(e)) show a compositional contrast within Ti_3SiC_2 regions: dark areas are Si-rich, while bright areas are Ti-rich. This heterogeneity likely results from intergranular Si segregation or outward diffusion of Si during sintering, while the higher atomic number of Ti enhances backscattered electron contrast. Elemental mapping (Fig. 4(b1)–(b6)) confirms the relatively uniform dispersion of Fe, Cu, and Ni, whereas Ti, Si, and C are mainly confined to Ti_3SiC_2 particles, highlighting the localized nature of the reinforcement phase. The magnified Cu region (Fig. 4(c)) and its corresponding EDS line scan (Fig. 4(d)) reveal negligible levels of Ti, Si, C, and Fe within the Cu phase, while Ni concentration is notably

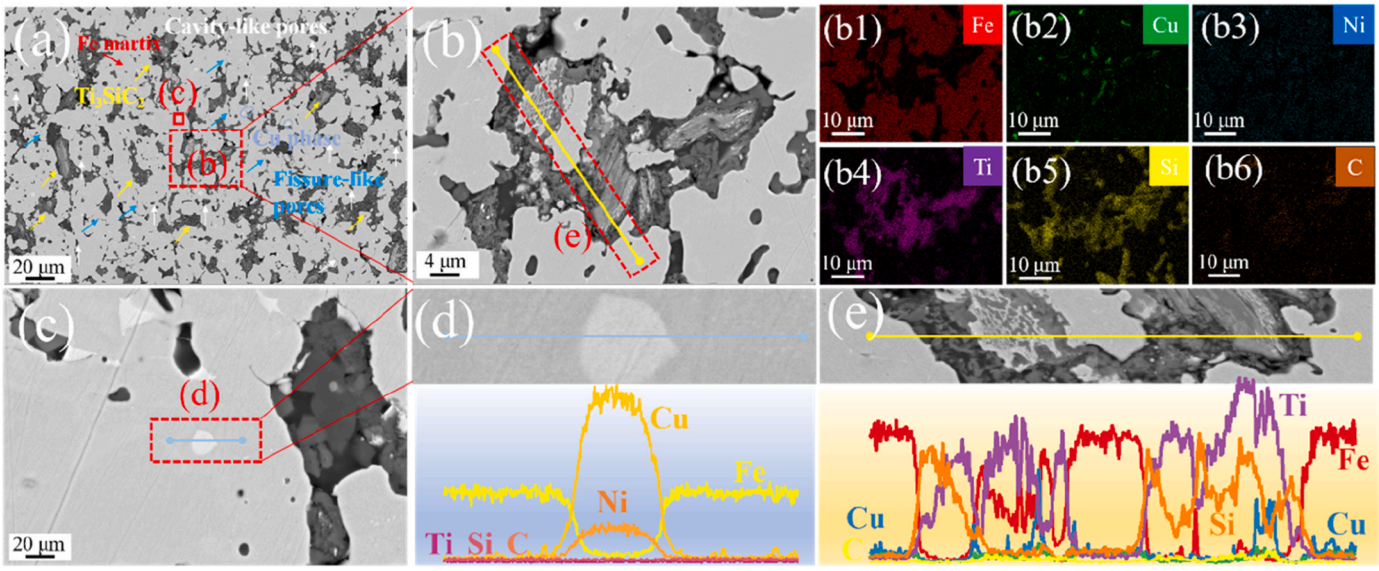

Fig. 4. (a) Surface morphology of 1Ni porous composite material, (b) magnified morphology of Ti_3SiC_2 in (a), (b1-b6) element distribution in (b), (c) magnified morphology of surface Cu phase in (a), (d) line scan image of Cu phase and its interface in (c) (e) is the line scan image of Ti_3SiC_2 and its interface in (b).

high. This is due to the complete miscibility of the Ni–Cu system, which favors the formation of a solid solution, contributing to strengthening. In contrast, the limited solubility of Fe in Cu and the strong affinity of Ti, Si, and C toward MAX phase stability result in their exclusion from the Cu-rich regions.

The surface morphology of the Fe-7.5Cu-3.0Ni-1.0GNP(Cu)–6Ti_3SiC_2 composite (Fig. 5(a)) shows a multiphase structure and defect features similar to the 1.0Ni sample. Cavity-like pores, indicated by white arrows, primarily result from the release of residual gases between the powders during rapid microwave heating and the limited diffusion time, leading to the retention of vacancies. Fissure-like pores, pointed out by blue arrows, are caused by microcrack propagation due to residual stresses induced by thermal expansion mismatch between Ti_3SiC_2 and the matrix. Ti_3SiC_2 particles, marked by yellow arrows, have a size range of 10–30 μm, and are uniformly distributed; however, a thin reaction layer may exist at the interface. In the magnified view of Fig. 5(b), EDS point scanning reveals that Ti_3SiC_2 partially decomposes during microwave sintering at 1100 °C (specific results are shown in Table 1). Point 1, with high Si (43.53 at.%) and C (46.24 at.%) content and low Ti (8.6 at.%), suggests the formation of a SiC-rich phase. This could be due to the volatilization of Si atoms from the MAX phase or their diffusion to the surface. Points 2 and 4 reveal constituents indicative of the transition phase or partial decomposition of Ti_3SiC_2. This deviation from the stoichiometric ratio of standard Ti_3SiC_2 (Ti:Si:C ≈ 50:17:33 at.%) may stem from local overheating effects during microwave sintering, which accelerate the desiliconization process rather than directly causing carbon to be substituted by silicon. In the layered MAX-phase structure of Ti_3SiC_2, composed of alternating stacks of Ti_6C octahedra and Si A-layers, the weakly bonded Si atoms tend to diffuse outward or volatilize preferentially due to their high vapor pressure, leading to structural collapse and the formation of TiC-rich regions (where residual carbon atoms coordinated octahedrally with Ti render the Ti:C ratio nearly equimolar). The liberated silicon may react with available carbon to form silicon carbide, which can be observed in silicon-rich regions. Such surface-initiated decomposition is triggered at approximately 1000–1300 °C under rapid heating, consistent with our microwave conditions and partial phase transitions (toward titanium carbide and silicon carbide), and it does not alter the octahedral carbon sites.Point 3, with near-equal amounts of Ti (48.87 at.%) and C (49.64 at.%), corresponds to a TiC phase, formed by the desiliconization decomposition of Ti_3SiC_2. Although this decomposition weakens the self-lubricating effect of the MAX phase, TiC contributes additional hardening, enhancing the wear resistance of the composite [33]. When the Ni content increases to 5.0 wt%, the surface morphology remains consistent (Fig. 5(c)), and there is no significant change in the density of cavity-like or fissure-like pores, indicating that Ni alloying mainly influences solid solution behavior rather than pore formation. The magnified view in Fig. 5(d) shows that GNPs are partially embedded in pores, likely due to the aggregation or migration of the GNP(Cu) layered structure during ball milling and sintering. Their low density prevents full dispersion under the microwave field, resulting in local densification issues. During cooling, thermal stress further fixes GNPs at the edges of the pores. Fig. 5 (e) shows the distribution of carbon in the pores. For the Ni = 7.0 wt% sample, the morphology in Fig. 5(f) indicates a more stable and uniform distribution of the reinforcing phases. The elemental distribution curves for Ti in the EDS scans (Fig. 5(f1)-(f6)) show a high degree of similarity to those of other Ni-content samples, as Ti_3SiC_2, acting as a ceramic filler, remains stable and unaffected by Ni alloying. Ni preferentially dissolves into the Fe–Cu matrix to form solid solution strengthening, rather than reacting with the MAX phase, thereby maintaining the uniform dispersion and consistency of the Ti_3SiC_2 particles. This similar distribution ensures that the composite maintains a comparable microstructure across different Ni levels. However, excessively high Ni content could potentially lead to the precipitation of secondary phases, which may negatively impact the overall mechanical properties.

3.2.3. *TEM microstructure analysis*

The microstructure of the Fe-7.5Cu–7Ni-1.0GNP(Cu)–6Ti_3SiC_2 porous laminated composite was observed using transmission electron microscopy (TEM). Fig. 6(a) shows a typical bright-field TEM image of Cu grains in the Fe matrix, which appear nearly spherical with sizes ranging from 50 to 80 nm and are highly dispersed within the matrix. No significant stacking or agglomeration is observed. The rapid surface diffusion and spherical reconstruction of Cu particles during microwave sintering are facilitated by the volumetric heating effect. Additionally, the copper coating on the GNPs may act as a surfactant, further reducing surface energy between Cu grains and preventing agglomeration. In comparison to conventional sintering, the non-equilibrium heating provided by the microwave process reduces excessive Cu grain growth, ensuring nanometer-scale uniformity [34]. Fig. 6(b) is an enlarged view of a single Cu grain from Fig. 6(a), approximately 60 nm in size, with a smooth surface and no visible crystal defects, indicating effective

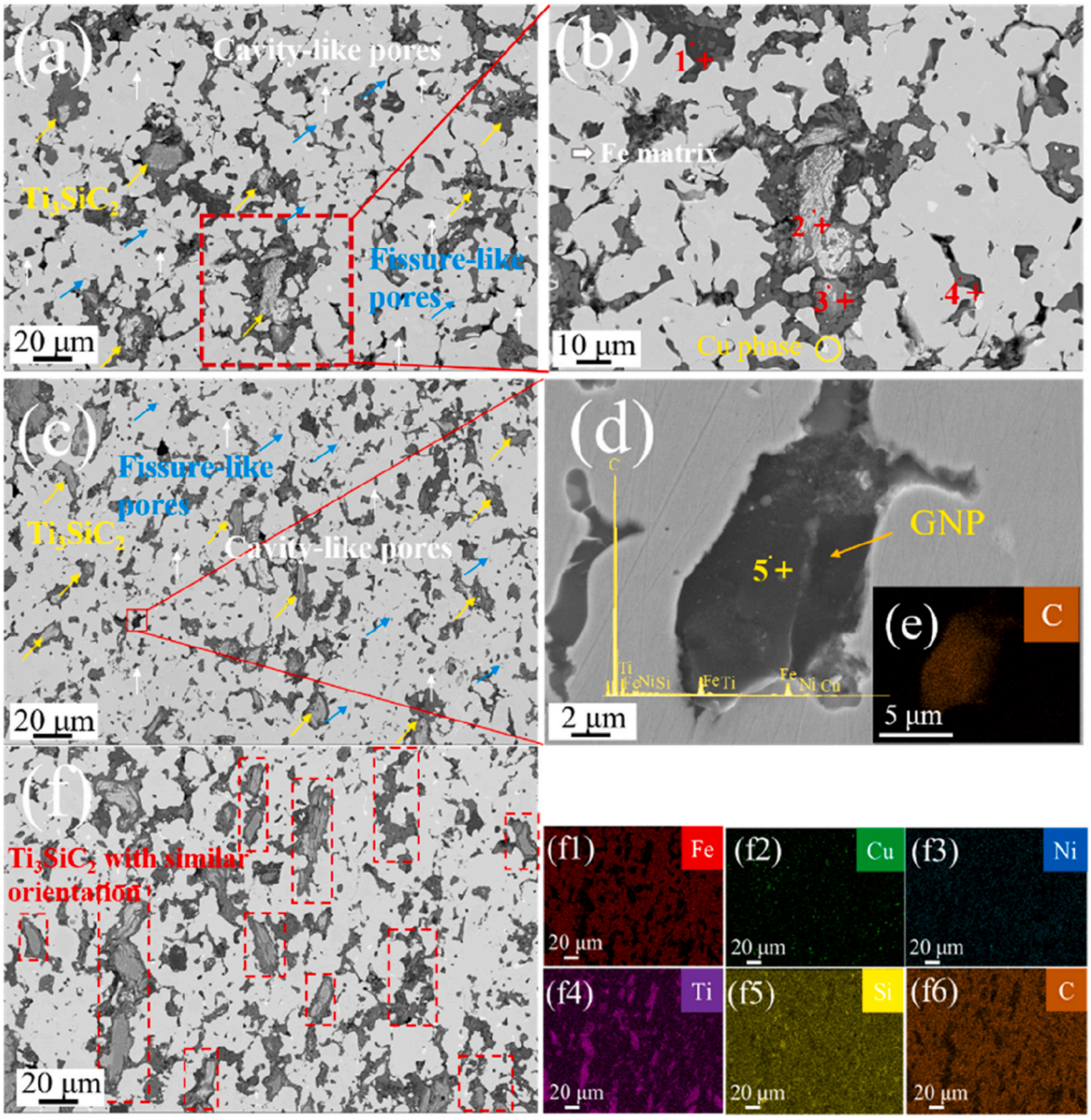

Fig. 5. (a) Surface morphology of 3Ni porous composite material, (b) is the enlarged image in the red box in (a), (c) surface morphology of 5Ni porous composite material, (d) GNP in the pores, (e) distribution map of C element in Fig. (d), (f) surface morphology of 5Ni porous composite material (f1-f6) represent the distribution of various elements in Fig. (f).

Table 1
Energy spectrum analysis of different points in the Ti_3SiC_2 phase in Fig. 5(b).

EDS points	Element(at.%)					
	Fe	Cu	Ni	Ti	Si	C
Spectrum 1	1.49 %	0	0.15 %	8.60 %	43.53 %	46.24 %
Spectrum 2	3.84 %	0.13 %	0.07 %	34.30 %	32.67 %	28.99 %
Spectrum 3	5.38 %	0.27 %	0.24 %	43.80 %	26.12 %	24.19 %
Spectrum 4	0.92 %	0.20 %	0.03 %	48.87 %	0.34 %	49.64 %

crystallization during the sintering process. The EDS mapping results in Fig. 6(b1)-(b6) show that Fe is concentrated in the matrix, forming the continuous phase; Cu is highly concentrated within the grains, confirming that Cu exists as a separate phase. Ni is evenly distributed at the Fe–Cu grain boundaries, likely forming Fe–Ni or Cu–Ni solid solutions, enhancing strengthening at the interfaces. Ti and Si are uniformly distributed, corresponding to the residual or decomposed Ti_3SiC_2 particles, and C is dispersed throughout the matrix, suggesting that graphene carbon layers or carbon from Ti_3SiC_2 have partially diffused and participated in reactions. Fig. 6(c) reveals a significant presence of Fe_3C phases in the composite, appearing as banded structures with widths of 20–50 nm and lengths reaching several hundred nanometers, aligned nearly parallel. This highly ordered, layered arrangement results from a non-equilibrium phase transition driven by multiple factors. During sintering, GNPs and Ti_3SiC_2 release free carbon atoms, which react with the Fe matrix to form Fe_3C. The rapid heating rate and selective absorption of microwaves (strong response of metal powders to 2.45 GHz microwaves) create local high-temperature gradients and electromagnetic stress fields. These effects induce carbon atom diffusion in specific directions, leading to preferential nucleation of Fe_3C on the Fe matrix lattice [35]. From a crystallographic and kinetic perspective, the FCC structure of the Fe matrix (with the [1 1 1] direction as the slip plane) guides the epitaxial growth of Fe_3C along low-mismatch crystal planes (e.g., (0 1 1) or (1 0 1)), forming banded precipitates [36]. This process is similar to directional solidification, where columnar crystals

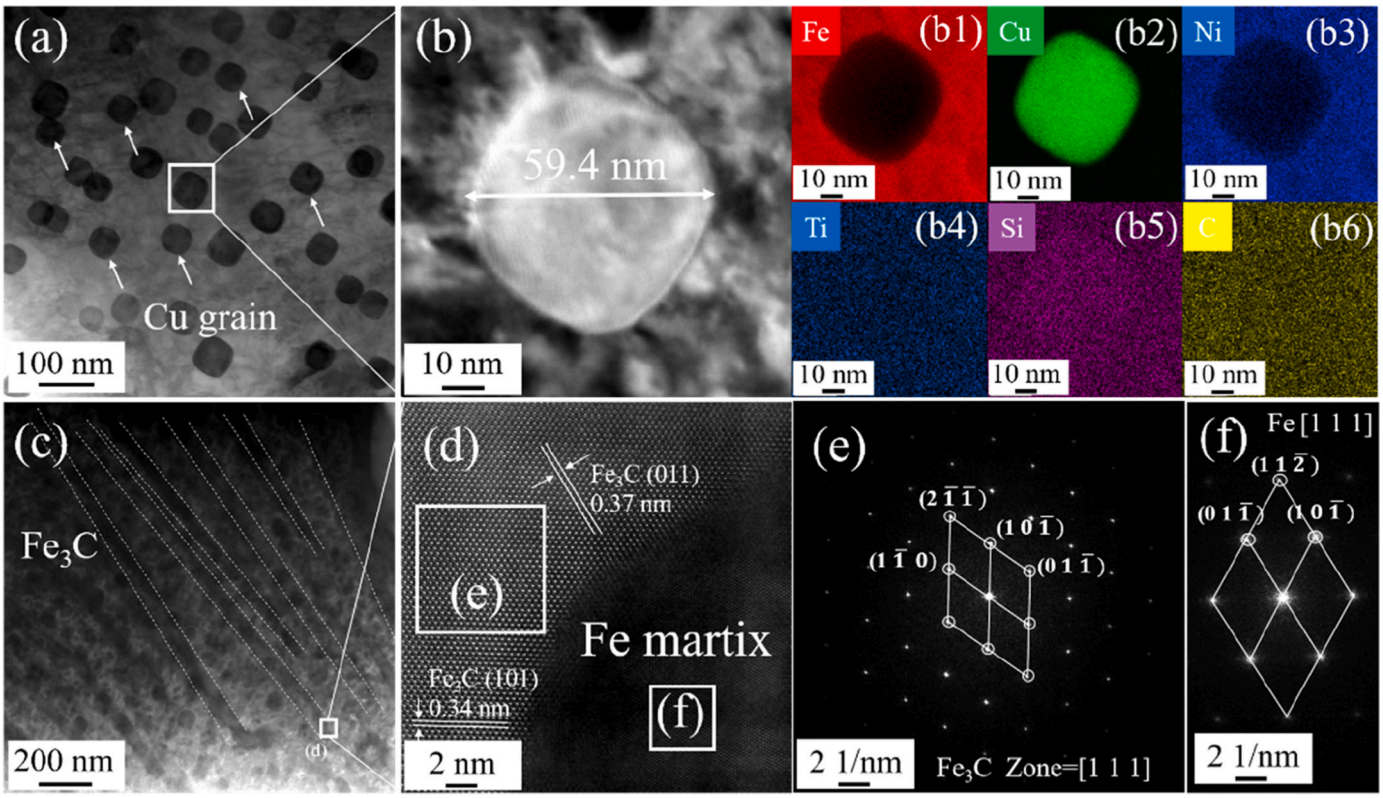

Fig. 6. TEM image of the 7Ni sample. (a) Cu phase in Fe matrix, (b) morphology of Cu grains after magnification, (b1-b6) as shown in Fig. (b). distribution of each element, (c) Fe_3C phase in Fe matrix, (d) HRTEM image at the interface between Fe_3C and Fe matrix, (e) selected electron diffraction image of Fe_3C, (f) selected electron diffraction image of Fe matrix.

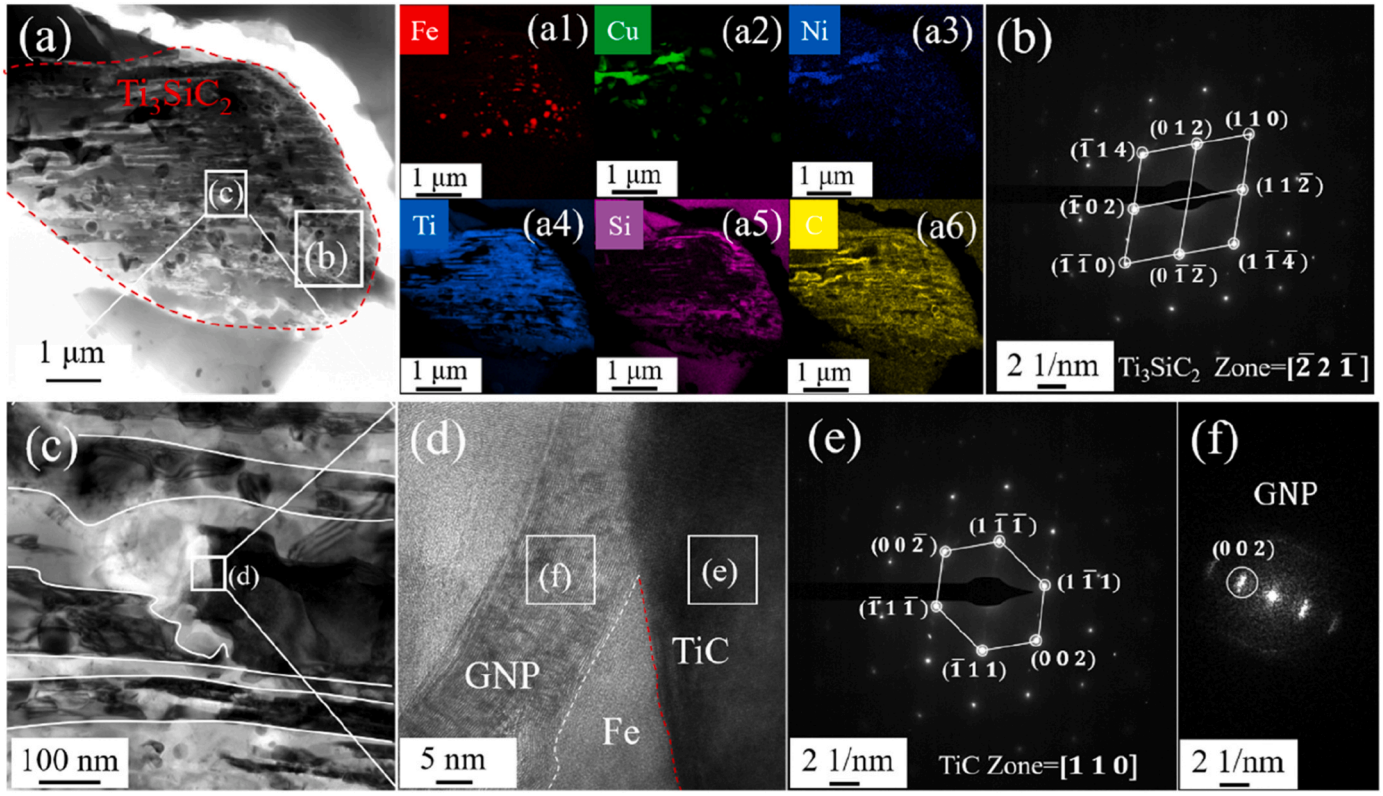

Fig. 7. (a) Ti_3SiC_2 phase in the Fe matrix, (a1-a4) shows the distribution of each element in Fig. (a), (b) is the selected area electron diffraction image of Ti_3SiC_2 in Fig. (a), (c) is the magnified topography of the c region in Fig. (a), and (d) is the high-resolution image at the interface in the d region in fig. (c). (e) is the selected electron diffraction image of TiC in Fig. (d), and (f) is the selected electron diffraction image of GNP in Fig. (d).

grow under the influence of temperature gradients and stress fields. Fig. 6(d) shows a high-resolution TEM image of the Fe–Fe_3C interface, revealing clear lattice fringes and atomic arrangements. The measured interplanar spacings of Fe_3C are 0.37 nm for the (0 1 1) plane and 0.34 nm for the (1 0 1) plane, in agreement with the theoretical values for the orthorhombic structure of Fe_3C, indicating high purity and crystallinity. No amorphous layers or transitional phases are observed at the interface. The low crystal mismatch between the FCC lattice of Fe and the orthorhombic structure of Fe_3C along the [1 1 1] direction allows for the direct incorporation of carbon atoms into the Fe lattice, forming ordered precipitates. This strong interface enhances load transfer efficiency; however, the interface stress could induce local dislocation accumulation, potentially affecting the material's cyclic stability. Fig. 6(e) and (f) show selected area electron diffraction (SAED) patterns for Fe_3C and Fe phases along the [1 1 1] crystal direction. The sharp diffraction spots indicate high crystallinity in both phases.

Fig. 7(a) shows the typical morphology of Ti_3SiC_2 particles, which exhibit a clear layered structure with a layer thickness of approximately 30–80 nm, characteristic of the MAX phase (Mn+1AXn) nanoscale crystal structure (alternating Ti and SiC layers). This layered morphology is largely preserved under microwave sintering, although slight peeling at the edges is observed, likely due to structural instability caused by Si atom volatilization at high temperatures. Black particulate matter on the surface, identified by EDS as Fe particles and Cu–Ni alloys, suggests that during sintering, matrix elements diffuse to the Ti_3SiC_2 surface, forming composite interfaces. The EDS mapping results in Fig. 7 (a1)-(a6) show that the Ti, Si, and C elements are evenly distributed, with Ti and Si concentrated in the core of the particles and C dispersed between the layers, confirming the chemical integrity of the Ti_3SiC_2 phase. Fe, Cu, and Ni are locally enriched on the surface of the particles, and as the Ni content increases, the Cu–Ni alloy region also expands. This is likely due to Ni promoting the solid solution and diffusion of Cu, improving the surface wettability of the particles. The uniform elemental distribution indicates that the volumetric effect of microwave heating suppresses phase separation. However, partial decomposition of Ti_3SiC_2 releases C and Si, affecting the formation of adjacent phases.

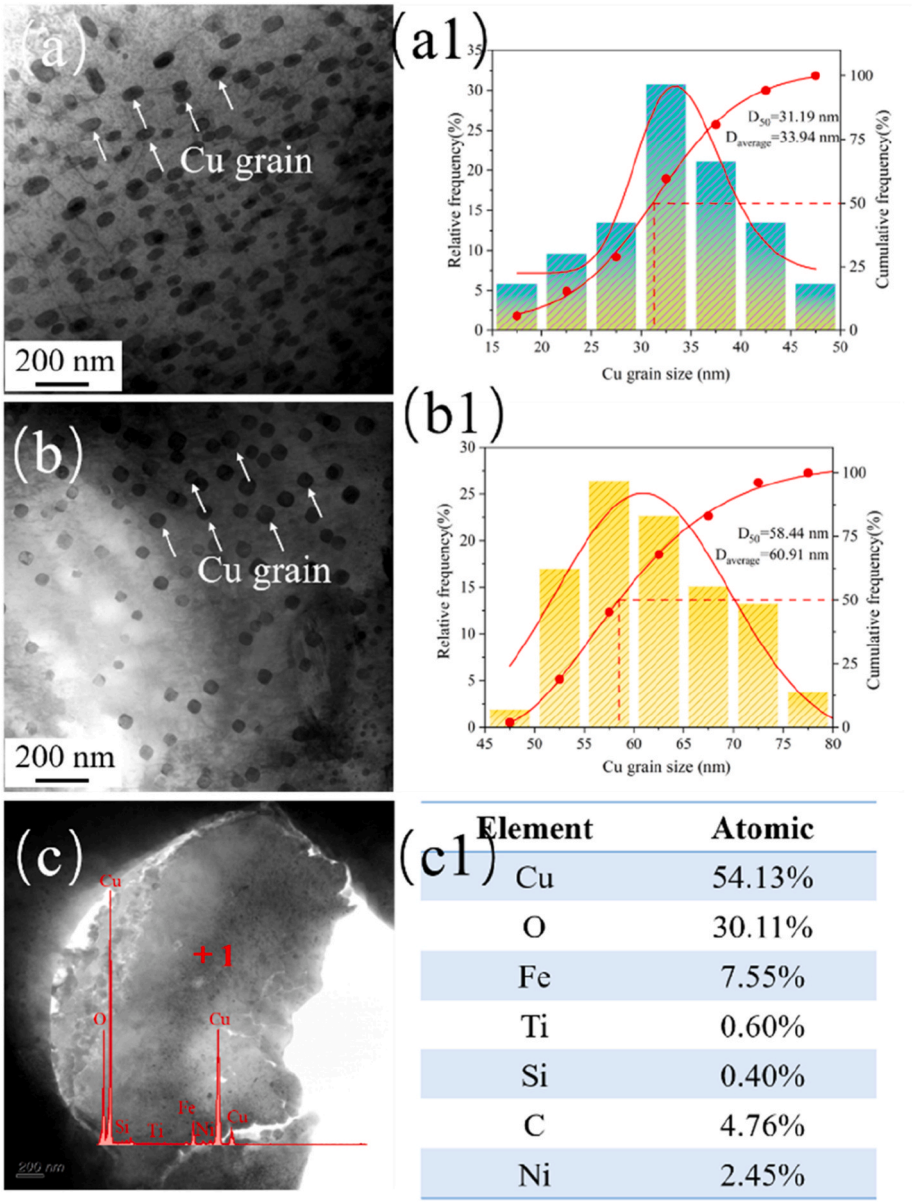

Element	Atomic
Cu	54.13%
O	30.11%
Fe	7.55%
Ti	0.60%
Si	0.40%
C	4.76%
Ni	2.45%

Fig. 8. (a) Cu grain morphology in the Fe matrix of the sample without Ni element added, (a1) Cu grain size distribution in the Fe matrix of the sample without Ni element added, (b) Cu grain morphology in the Fe matrix of the sample with 7Ni element added, (b1) Cu grain size distribution in the Fe matrix of the sample with 7Ni element added (c) Morphology and point scan energy spectrum of sheet-like substances in the pores, (c1) atomic ratio of each element in the point scan region.

Fig. 7(b) shows the selected area electron diffraction (SAED) pattern of region b from Fig. 7(a), with the diffraction spots arranged symmetrically along the [$\bar{2}\,2\,\bar{1}$] crystal axis, corresponding to the hexagonal crystal structure of Ti_3SiC_2. The sharp, clear diffraction spots with no diffuse rings indicate high crystallinity, and microwave rapid heating preserves the layered symmetry of the MAX phase. Fig. 7(c) provides a magnified image of region c from Fig. 7(a), clearly showing the layered structure and alternating color contrast between the two phases. The interlayer spacing is approximately 20–60 nm, and the edges exhibit peeling induced by thermal stress, further supporting the nanolayered nature of Ti_3SiC_2. This contrast is due to differences in electron density, indicating the role of Ti_3SiC_2's nanoscale layered structure as a lubricating phase that enhances material strength and toughness during sintering. Fig. 7(d) presents a high-resolution TEM (HRTEM) image focused on region d in Fig. 7(c), showing the interface between the GNP, Fe matrix, and TiC phases. The GNP is embedded as thin sheets within the Fe matrix, while TiC appears as nanoparticles at the interface. The interface between the three phases is well-bonded and clean, with no impurities or amorphous layers, indicating good phase compatibility. Fig. 7(e) shows the SAED pattern for the TiC region, with diffraction spots symmetrical along the [1 1 0] axis, confirming the cubic crystal structure of TiC, which results from the high-temperature decomposition of Ti_3SiC_2. Fig. 7(f) presents the SAED pattern for the GNP region, also along the [1 1 0] axis, corresponding to the honeycomb structure of the GNPs. The copper coating likely stabilizes the crystallization of the GNPs, with no defects observed.

The effect of Ni addition on the Cu grain size distribution in the composites was investigated using TEM. As shown in Fig. 8(a), in the Ni-free system, Cu grains exhibit nanoscale dispersion (approximately 20–50 nm), with uniform distribution and high density. Size distribution statistics in Fig. 8(a1) indicate $D_{50} = 31.19$ nm and $D_{average} = 33.94$ nm, suggesting that in the absence of Ni, Cu grains are fine and densely distributed. This is primarily due to the rapid heating of microwave sintering, which limits Cu diffusion. In contrast, as shown in Fig. 8(b) and (b1), adding 7 wt% Ni leads to significant coarsening of Cu grains, with $D_{50} = 58.44$ nm and $D_{average} = 60.91$ nm. This grain growth is attributed to the unlimited solubility between Ni and Cu, leading to solid solution formation. The smaller atomic radius of Ni (0.124 nm) compared to Cu (0.128 nm) induces lattice distortion and solid solution strengthening, reducing the surface energy of Cu particles and enhancing atomic diffusion. This facilitates grain coalescence and recrystallization during sintering. Additionally, Ni promotes alloying within the Fe–Cu–Ni system. Its magnetic behavior under microwave fields enhances local heating, selectively facilitating the formation of a Cu liquid phase and stabilizing nuclei, nearly doubling the grain size [37]. Moreover, Ni suppresses Cu oxidation due to its higher oxidation potential, further promoting grain growth. However, excessive Ni may induce phase separation, adversely affecting compositional uniformity [38]. The addition of Ni positively influences mechanical properties, primarily through solid solution strengthening, improved microstructure, and enhanced interfacial bonding. Ni also increases density and hardness, and Ni-rich regions help inhibit crack propagation. Fig. 8(c) shows flaky substances within the pores. EDS point analysis in Fig. 8(c1) reveals an oxygen content of 30.11 at.%, indicating the possible formation of metal oxides. During microwave sintering, these closed pores retain trapped oxygen, which reacts with exposed Cu powder to form

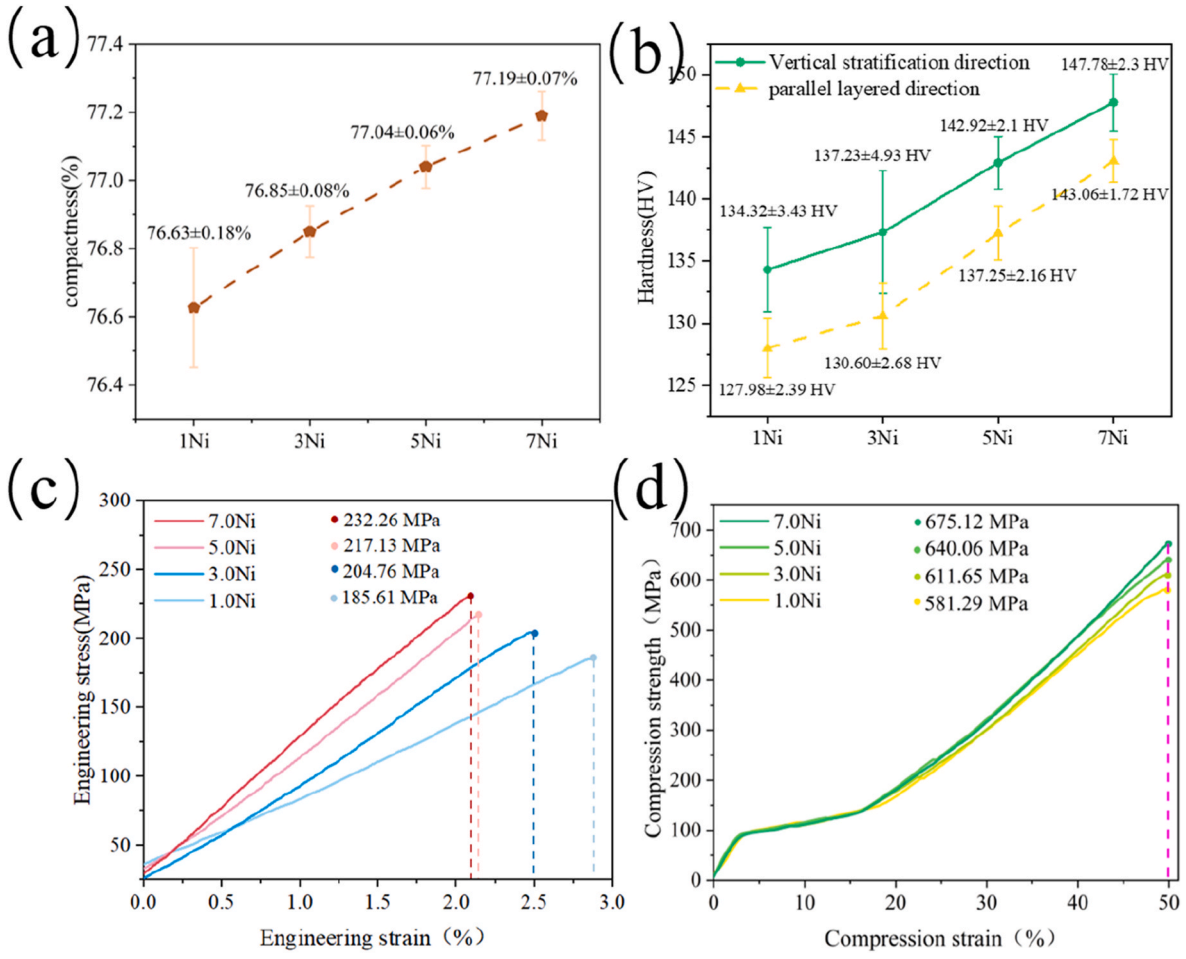

Fig. 9. Mechanical properties of four composite materials. (a) Density, (b) Hardness perpendicular or parallel to the layered direction, (c) engineering stress-strain curve of the composite material, (d) compressive stress-strain curve of the composite material.

oxides such as CuO. However, Ni addition can partially mitigate this effect by increasing the oxidation barrier, thereby inhibiting Cu oxidation, stabilizing interfaces, and enhancing overall hardness and fatigue life [39].

3.3. Mechanical property testing

Fig. 9(a) shows that the relative density gradually increases with rising Ni content, from 76.63 ± 0.18 % to 77.19 ± 0.07 %, with a total increase of approximately 0.7 %. This trend is primarily attributed to the diffusion activation effect of Ni in the Fe–Cu system: Ni forms a fully miscible solid solution with Cu, enhancing the wettability and diffusion coefficient of the Cu liquid phase, thereby suppressing sintering expansion caused by Cu penetration into Fe grain boundaries. It also promotes neck formation and pore closure between powder particles. The observed reduction in cavity-like pores under SEM further confirms that Ni improves powder homogeneity. Together with the nanofiller effect of GNPs and the anchoring effect of the Ti_3SiC_2 ceramic phase, Ni helps suppress residual porosity by pinning grain boundaries. However, excessive Ni may lead to Ni phase precipitation, causing non-uniform expansion and potential drawbacks.

As shown in Fig. 9(b), the hardness increases with rising Ni content: when the Ni content reaches 7 %, the hardness parallel to the layered direction is 143.06 ± 1.72 HV, and the hardness perpendicular to the layers reaches 147.78 ± 2.3 HV, representing an overall increase of approximately 10 % and indicating slight mechanical anisotropy. This may be attributed to the larger contact area of GNPs in the direction perpendicular to the layers, which better distributes the applied pressure. Similarly, during compression, the force is applied in the same direction, allowing the dispersed GNPs to more effectively share the load; thus, it can be inferred that compressive strength perpendicular to the layers is likely higher than that parallel to the layers. In contrast, the tensile strength is higher when measured parallel to the layered direction than perpendicular to it, due to the greater load-transfer capability of GNPs aligned along the layers. Therefore, it can be inferred that under tensile loading, the tensile strength perpendicular to the layered structure is lower than that parallel to it [40].

The engineering stress–strain curves in Fig. 9(c) show that the tensile strength increases from 185.61 MPa to 232.26 MPa, while the elongation decreases from 2.875 % to 2.09 %. The improvement in strength is mainly due to solid solution strengthening and grain refinement, which raise the yield point. Crack deflection is further promoted by GNP bridging and Ti_3SiC_2 layer cleavage, improving load transfer. The reduction in elongation reflects the typical strength–ductility trade-off, as increased lattice strain with higher Ni content limits plastic deformation. Nonetheless, the self-lubricating nature of Ti_3SiC_2 and the toughening effect of GNPs maintain reasonable ductility. The slope of the stress–strain curve increases with rising Ni content, indicating stronger atomic bonding and reduced elastic deformability due to lattice contraction [41].

Fig. 9(d) shows that the compressive strength at 50 % strain increases from 581.29 MPa to 675.12 MPa with increasing Ni content. Similar to the tensile response, Ni strengthens the matrix and suppresses plastic collapse, while Ti_3SiC_2 and GNP(Cu) contribute to load-bearing through dispersed reinforcement. The plateau observed in the curves reflects the typical behavior of porous materials: after the initial elastic region, pore collapse and layered structural sliding stabilize the stress response, resembling the energy absorption plateau of cellular materials. In this regime, residual pore collapse dissipates energy. The addition of Ni shortens the plateau and increases peak strength, indicating improved pore distribution and interfacial toughness.

Although the primary strengthening effects arise from the microstructural role of nickel (solid-solution strengthening and grain refinement), the porous nature of the composites necessitates explicit consideration of densification. With increasing Ni content, the wettability and diffusivity of Cu are enhanced, leading to an approximate 0.56 % increase in relative density, thereby reducing cavity-like pores and alleviating stress concentration. According to the Gibson–Ashby model for open-cell porous metals [42], the compressive strength follows the relation $\sigma \propto \rho^{\frac{3}{2}}$, whereby this density change alone can result in an approximately 1.1 % increase in strength; optimizing sintering parameters to achieve densification can thus limit pore-induced failure and improve mechanical performance. This effect works synergistically with the overall strengthening mechanisms, maintaining the porosity required for functional applications while simultaneously enhancing load-bearing capacity.

The research results were compared with established benchmarks of similar porous alloys used in frictional applications (such as bearings and gears). Reference was made to ASTM B438 (applicable to oil-impregnated sintered bronze-based powder metallurgy bearings), which specifies a minimum tensile strength of 138–241 MPa for unreinforced Cu–Sn alloys and a compressive strength up to 345 MPa [43,44]. Recent data on Fe–Cu porous alloys [45] were also cited (e.g., unreinforced Fe–7.5Cu alloys typically exhibit tensile strengths of 150–180 MPa and compressive strengths of 400–500 MPa). The optimized 7 % Ni composite exhibits superior performance: a tensile strength of 232.3 MPa (25.13 % higher than the 1 wt% baseline value) and a compressive strength of 675.1 MPa (an increase of 16.14 %). While maintaining a porosity of approximately 23 % to facilitate lubrication, it demonstrates strong potential for applications under demanding conditions.

Fig. 10(a) shows the fracture morphology of Fe-7.5Cu-1.0Ni-1.0GNP (Cu)–6Ti_3SiC_2 composite, revealing a layered structure primarily resulting from the orientation of flake-shaped Fe powders during cold pressing and microwave sintering. This forms a shell-like architecture that enhances anisotropic strength and crack resistance. Pores are also present, caused by incomplete closure of powder interstices. Fig. 10(b) reveals that Ti_3SiC_2, sandwiched between Fe layers, exhibits a lamellar structure characteristic of MAX-phase nanoscale crystals. The weakly bonded Si layers are prone to stress-induced cleavage, resulting in a peeling morphology. The dimple size ranges from 1 to 6 μm, indicating brittle-ductile mixed fracture with microvoid nucleation and growth as the primary mechanism. The Ti distribution in Fig. 10(b1) confirms the presence and morphology of the Ti_3SiC_2 powder. When Ni content increases to 3.0 wt%, the fracture morphology in Fig. 10(c) retains the layered and porous features. Fig. 10(d) confirms by point scanning that GNPs are embedded in the pits, accompanied by Cu particle precipitation. This is likely due to the flow of the Cu liquid phase filling the microvoids between Fe matrix particles, relieving stress. The Cu soft phase absorbs energy, suppresses crack propagation, and enhances ductility. The partial enrichment of Cu is attributed to its high diffusion rate and compatibility, similar to the pinning effect of a secondary phase, which improves toughness. When Ni content reaches 5.0 wt%, Fig. 10(e) shows a similar layered morphology. Fig. 10(f) shows the observed pulled GNPs, which dissipate fracture energy through decohesion and bridging, improving toughness, preventing catastrophic fracture, and optimizing fatigue resistance. At 7 wt% Ni, Fig. 10(g) still shows a layered structure with pore-induced dimples. Ni does not disrupt the structure but may fine-tune the matrix through solid solution strengthening. Fig. 10(g1)-(g6). EDS mapping shows uniform dispersion of Fe, Cu, and Ni, with Ti, Si, and C primarily confined to the Ti_3SiC_2 phase. Ni enriches the Cu phase, promoting solid solution formation and improving ductility. Elemental segregation occurs due to Ni's inhibition of diffusion, preventing reactions and maintaining stable optimized mechanics. Although high Ni content may locally induce brittleness, it contributes to overall toughness enhancement [46]. Overall, as Ni content increases, it helps reinforce the matrix and optimize the interface, enhancing overall performance. However, its content must be controlled to avoid brittle transformation.

Although composite materials designed with sheet-like powder metallurgy techniques exhibit a biomimetic nacreous layered structure,

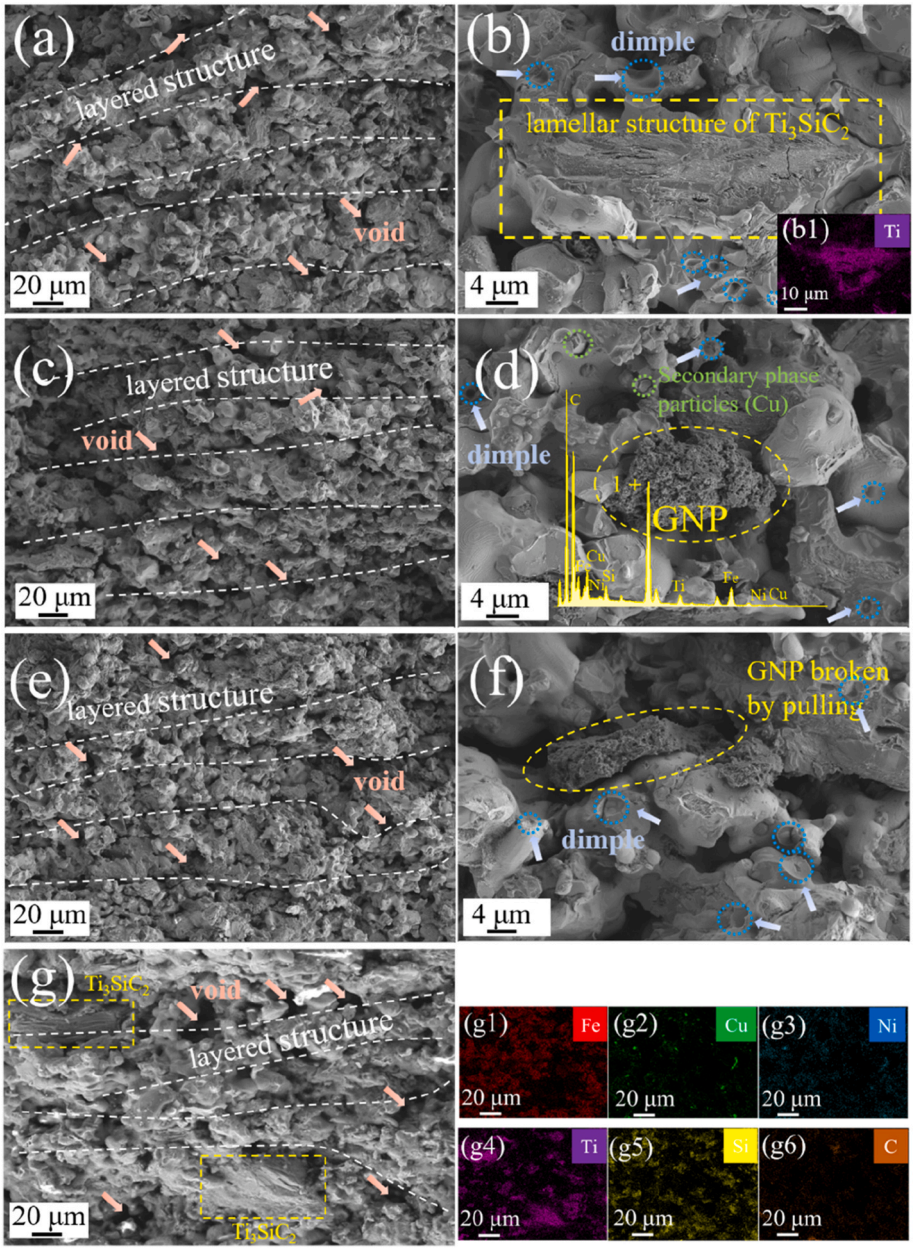

Fig. 10. (a) Fracture morphology diagram of 1Ni composite material, (b) Ti_3SiC_2 in Fe phase, (b1) Ti element distribution in Fig. (b), (c) fracture morphology diagram of 3Ni composite material, (d) GNP in Fe phase, (e) fracture morphology diagram of 5Ni composite material, (f) GNP broken by drawing. (g) Fracture morphology diagram of 7Ni composite material, (g1-g6) is the distribution diagram of each element in Fig. (g).

during cold pressing the sheet-like Fe and Cu powders arrange to form alternating layers reinforced by GNP(Cu) and Ti_3SiC_2. However, this layered architecture tends to be clearly discernible in fracture SEM images, with multiple factors potentially obscuring the layered structure: (1) Fracture surfaces often propagate at angles non-parallel to the layered planes, along intergranular or transgranular directions, resulting in stepped or irregular surfaces rather than flat cross-sections; (2) The presence of pores, pits, and pulled-out reinforcements (e.g., fractured GNPs, Ti_3SiC_2 layers) introduces surface roughness and artefacts, obscuring the underlying stacked structure; (3) Decomposition products like TiC and elemental distribution increase multiphase complexity, diverting visual focus from the matrix layers; (4) Microwave sintering preserves anisotropic pores and phase interfaces, which, while promoting crack deflection along layers, result in complex fracture paths partially obscuring the layered sequence; (5) Melting and flow of lamellar copper during high-temperature sintering at 1100 °C partially diminish the layered structure.

3.4. Strengthening mechanisms

In the Fe-7.5Cu-xNi-1.0GNP(Cu)–6Ti_3SiC_2–7Ni composite, GNP serves as the carbon-based nanoreinforcement, Ti_3SiC_2 acts as the ceramic reinforcement, and Ni functions as the alloying element. Their synergistic interaction with the Fe–Cu matrix significantly enhances the overall mechanical performance of the material. In this study, although Ni content serves as the experimental variable, the individual contributions of GNP and Ti_3SiC_2 to the strength enhancement can be quantified through calculations. The theoretical yield strength (YS) of the composite can be estimated using the classic rule of mixtures (ROM) model (Equation (3)) [47]. However, the significant solid solution strengthening effect of the higher Ni content on the Fe matrix cannot be ignored in this experimental system. Therefore, the modified ROM

model, as shown in Equation (4), is applied.

$$\Delta\sigma_c = \Delta\sigma_{CTE} + \Delta\sigma_{GR} + \Delta\sigma_{load} + \Delta\sigma_{OR} \tag{3}$$

$$\Delta\sigma_c = \Delta\sigma_{ss} + \Delta\sigma_{CTE} + \Delta\sigma_{GR} + \Delta\sigma_{load} + \Delta\sigma_{OR} \tag{4}$$

$\Delta\sigma_{ss}$ represents the strengthening contribution from lattice distortion induced by Ni solid solution. $\Delta\sigma_{CTE}$ denotes the strengthening contribution due to dislocations caused by coefficient of thermal expansion (CTE) mismatch. $\Delta\sigma_{GR}$ corresponds to the strengthening contribution from grain refinement of the Fe matrix. $\Delta\sigma_{load}$ refers to the load transfer and dissipation strengthening contribution provided by the reinforcement particles. The Orowan strengthening effect, caused by dislocations bypassing the reinforcement particles, is also included in $\Delta\sigma_{load}$. Although the five strengthening models adopted in this work are derived from dense metal matrix composites, they remain applicable to porous systems such as the one studied here, as they primarily govern the interactions between the matrix and the reinforcement within the solid phase. Porosity regulates the overall strength by reducing the effective density, but it does not exclude the aforementioned strengthening mechanisms.

3.4.1. Solid solution strengthening

During the doping process, Ni atoms substitute into the Fe–Cu matrix lattice to form a substitutional solid solution. This process not only increases the solute atom concentration but also introduces lattice distortion caused by Ni atoms, generating localized elastic stress fields that significantly hinder dislocation glide and climb. A higher solute concentration effectively increases lattice friction stress, thereby enhancing the alloy's yield strength and resistance to plastic deformation, ultimately improving its overall mechanical properties. Moreover, the solid solution strengthening effect is positively correlated with Ni content, contributing to improved long-term material stability. The quantitative relationship between solute concentration and strengthening increment can be described using the Fleischer model [48].

$$\Delta\sigma_{ss} = MAG\varepsilon^{\frac{3}{2}}c^{\frac{1}{2}} \tag{5}$$

In the equation, $\Delta\sigma_{ss}$ represents the yield strength increment (MPa) resulting from solid solution strengthening. M is the Taylor factor (~3.06), and A is a constant typically taken as 0.08 for Fe–Ni alloys. G is the shear modulus of the matrix (~80 GPa), and ε is the lattice mismatch strain parameter (~0.004). c is the atomic fraction of solute (~0.07). Substituting the above values yields a solid solution strengthening increment of 17.30 MPa.

3.4.2. Fine-grain strengthening

After ball milling and mixing, Ni powder is doped and dispersed into the Fe–Cu matrix. This process not only homogenized the composite powder particles but also effectively suppressed grain growth during the subsequent microwave sintering process through solid solution strengthening by Ni. Smaller grain sizes significantly increase the volume fraction of grain boundaries, adding resistance to dislocation movement, thereby greatly improving the alloy's strength, hardness, and other mechanical properties. Furthermore, the grain boundary pinning effect induced by Ni further stabilizes the fine-grained structure. The relationship between grain size and mechanical properties can be quantitatively described by the Hall-Petch relationship [49].

$$\Delta\sigma_{GR} = K\left(D_c^{-0.5} - D_m^{-0.5}\right) \tag{6}$$

Where K is the Hall-Petch slope, reflecting the grain boundary's ability to hinder dislocation motion, and for Fe–Cu-based alloys, it is approximately 0.2 MPa $m^{1/2}$, where D_m and D_c represent the grain sizes before and after alloy modification, respectively. Substituting the grain sizes of 1 % Ni and 6 % Ni alloys into the equation yields a $\Delta\sigma_{GR}$ value of 32.06 MPa.

3.4.3. Load transfer

Through the lamination process of flake powders, flake-shaped GNP (Cu) and Fe powders are arranged in an ordered fashion, increasing the interfacial contact area and enhancing the orientation consistency of GNP(Cu). Benefiting from the excellent tensile strength of GNP(Cu), this configuration enables effective stress transfer from the matrix to GNP (Cu) under load, forming a "skeleton-matrix" type reinforcing structure that significantly enhances the mechanical properties of the composite. In addition, Ti_3SiC_2, as a reinforcing phase with a certain aspect ratio, also facilitates the transfer of stress from the matrix to the reinforcing phase. The contribution of this mechanism to the material's strength can be quantitatively analyzed using the following equation [50].

$$\Delta\sigma_c = \sigma_m\left[\frac{(s+4)V_f}{4} + (1 - V_f) - 1\right] \tag{7}$$

Where σ_m denotes the yield strength of the Fe matrix (~130 MPa), s is the aspect ratio of the filler, and V_f is the volume fraction of the filler, with GNP and Ti_3SiC_2 being the fillers used in this study. The aspect ratios of GNP and Ti_3SiC_2 were statistically determined using SEM, yielding values of 26.71 and 2.69, respectively. Using the Jade 9 software and the internal standard method based on peak intensity, the phase ratios of Fe_3C and Ti_3SiC_2 relative to the reference phase (Cu) were calculated, determining the volume fractions of GNP (~0.58 %) and Ti_3SiC_2 (~8.72 %). Substituting these values into the calculation yields contribution values of 5.03 MPa and 7.62 MPa for GNP and Ti_3SiC_2, respectively.

3.4.4. Orowan strengthening

The Orowan strengthening mechanism involves the introduction of hard particles at the micron or nanometer scale as the reinforcing phase, which, under external loading, can hinder the motion of dislocations due to their dispersed distribution, thereby enabling effective stress distribution and, to some extent, suppressing crack propagation. However, when two-dimensional phases with high aspect ratios are used as reinforcement, the effect of this mechanism is relatively limited and can generally be neglected. The mathematical description of this mechanism is as follows [51].

$$\Delta_{\sigma_{Orowan}} = \frac{0.4MGb}{\pi\sqrt{1-\nu}} \frac{\ln\left(\frac{\sqrt{\frac{2}{3}}r}{b}\right)}{\sqrt{\frac{2}{3}}r\left(\sqrt{\frac{\pi}{4V_p}} - 1\right)} \tag{8}$$

Here, M is the Taylor factor (~3.06), G is the shear modulus (~80 GPa), b represents the Burgers vector (~0.253 nm), and ν is the Poisson's ratio (~0.25). The variables r and V_p denote the average equivalent circular diameter and volume fraction of Fe_3C, Ti_3SiC_2, and TiC, respectively. Based on statistical analysis using SEM and TEM, r_{Fe_3C} and $V_{p_{Fe_3C}}$ are 359 nm and 0.341 %, respectively; $r_{Ti_3SiC_2}$ and $V_{p_{Ti_3SiC_2}}$ are 5.04 μm and 9.12 %, respectively; r_{TiC} and $V_{p_{TiC}}$ are 825 nm and 1.09 %, respectively; The calculated contributions to strength from Fe_3C, Ti_3SiC_2, and TiC are 14.51 MPa, 7.78 MPa, and 12.65 MPa, respectively, totaling 34.94 MPa.

3.4.5. Thermal mismatch strengthening

The significant mismatch in the thermal expansion coefficients between the Fe matrix and the reinforcement components (Ti_3SiC_2 and GNP) results in a noticeable difference in the shrinkage rates of different parts of the material during the cooling process after microwave sintering. This shrinkage inhomogeneity induces residual stresses at the phase interfaces, leading to the formation of dislocations near the matrix. These additional dislocations, generated under external loading, effectively block dislocation slip and propagation, thereby enhancing the material's resistance to plastic deformation and significantly

improving its overall strength. The quantification of this mechanism can be performed using Equation (9) [52].

$$\Delta\sigma_{CTE} = \alpha G_m b\sqrt{\frac{12V_p\Delta T\Delta CTE}{bd(1-V_p)}} \tag{9}$$

In this equation, α is the strengthening factor (~0.5), G_m represents the shear modulus of the α-Fe matrix (~47.5 GPa), b denotes the Burgers vector (~0.253 nm), ΔT refers to the temperature difference between the processing and the mold (~1075 K), d is the average particle size of each reinforcing phase, V_p is the volume fraction of the reinforcing phase, and ΔCTE indicates the difference in thermal expansion coefficients (CTE) between the matrix and the reinforcement phases. ($\Delta CTE_{Fe} = 12\times10^{-6}$/K, $\Delta CTE_{Ti_3SiC_2} = 9\times10^{-6}$/K, $\Delta CTE_{GNP} = -1\times10^{-6}$/K, $\Delta CTE_{TiC} = 7.4\times10^{-6}$/K, $\Delta CTE_{Fe_3C} = 7.0\times10^{-6}$/K). Substituting the above data yields thermal mismatch contributions of 10.45 MPa, 2.80 MPa, 10.63 MPa, and 9.37 MPa for Ti_3SiC_2, GNP, TiC, and Fe_3C, respectively, totaling 33.25 MPa.

The calculated values reveal the contributions of five main strengthening mechanisms to the yield strength (YS), with the strengthening effects ranked as follows: $\Delta_{\sigma_{Orowan}}$ (34.94 MPa)>$\Delta\sigma_{CTE}$ (33.25 MPa) >$\Delta\sigma_{GR}$ (32.06 MPa) >$\Delta\sigma_{ss}$ (17.33 MPa) >$\Delta\sigma_c$ (12.65 MPa). Among them, the Orowan strengthening mechanism has the largest contribution, followed by CTE and fine-grain strengthening, which are similar in magnitude. The primary reason is that the Orowan strengthening is maximized due to the uniform dispersion of Ti_3SiC_2 decomposing into TiC nanoparticles, which effectively hinder dislocation slip and form Orowan loops, while Ni promotes particle stability. CTE and fine-grain strengthening are similar and ranked next, as CTE strengthening induces an increased dislocation density at the interfaces during cooling due to thermal expansion mismatch, complementing the Hall-Petch effect of fine-grain strengthening, forming a cooperative dislocation-grain boundary barrier. However, it is not as directly efficient as particle strengthening. Solid solution strengthening is weaker due to the low Ni solubility content and the similar atomic radii of Fe and Ni, which results in atomic-level lattice distortion effects being easily masked by the particles [53,54]. The weakest load transfer occurs due to the low volume fractions of GNP(Cu) and Ti_3SiC_2 and weak interfaces that reduce the efficiency of stress transfer. Overall, dominated by reinforcing phase particles and influenced by the Ni variable, the particle dispersion mechanism is superior to solid solution and interface effects, thus optimizing the material's yield strength. Fig. 11 shows the contribution values of different components to the mechanical strengthening of the composite material. Fig. 12 schematically illustrates the operative strengthening mechanisms. Under the application of external force, solid-solution strengthening originates from nickel-induced lattice distortions that immobilize dislocations. Load transfer is achieved by efficiently shifting stress from the softer Fe–Cu matrix to the harder reinforcement phase. Orowan strengthening involves the formation of dislocation loops around dispersed phases (such as TiC generated from the decomposition of Ti_3SiC_2). During phase-transformation cooling, thermal mismatch generates additional dislocations at the phase interfaces. Grain refinement strengthening enhances yield strength through the densification of grain boundaries. These mechanisms collectively suppress crack propagation and enhance the overall performance of the porous structure.

4. Conclusion

In this study, a dual-reinforcement strategy was employed by incorporating 1 wt% carbon-based nanoscale reinforcement GNP(Cu) and 6 wt% ceramic reinforcement Ti_3SiC_2 into an Fe–7.5Cu matrix, with adjustments made through optimization of Ni content (1–7 wt.%). Using flake powder metallurgy combined with a 1100 °C microwave sintering process, Fe–7.5Cu–xNi–1GNP(Cu)–6Ti_3SiC_2 composites were fabricated, forming a biomimetic nacre-like layered structure with a porosity of approximately 23 %. Through tensile/compression testing, SEM/EDS analysis, and XRD characterization, the effects of Ni alloying on the microstructure and mechanical properties were systematically investigated, leading to the following conclusions.

1. The incorporation of flake-shaped Fe and Cu powders with a high specific surface area can significantly improve the geometric compatibility between GNP(Cu), Ti_3SiC_2, and the matrix powders. This enhancement in geometric compatibility not only facilitates the uniform distribution of the composite but also aids in controlling the orientation of GNP(Cu) and Ti_3SiC_2, supporting the formation of a layered structure. Inspired by the biomimetic design of nacre, this layered configuration contributes to the optimization of mechanical properties by refining the grains, reinforcing interfacial bonding, and expanding the interfacial area.
2. Ti_3SiC_2 and its decomposition product TiC, along with GNP and its reaction product Fe_3C, act as reinforcement phases at the nanoscale or microscale. The strengthening mechanisms within this system involve Orowan strengthening, load transfer strengthening, and thermal mismatch strengthening.
3. The hardness of the alloy exhibits anisotropy, attributable to the differing dispersion effects of GNP on forces applied perpendicular or parallel to the layered orientation.
4. When the Ni content reaches 7 wt%, the composite achieves its best overall performance, with a tensile strength of 232.26 MPa and a compressive strength of 675.12 MPa at 50 % strain—representing improvements of 25.13 % and 16.14 %, respectively—while plasticity decreases by 27.3 %. This is primarily attributed to the combined effects of Ni-induced solid solution strengthening and grain refinement in the matrix.
5. Ni alloying significantly increases the size of Cu precipitates. Given the complete solubility between Ni and Cu, and the smaller atomic radius of Ni compared to Cu, lattice distortion occurs, reducing surface energy and accelerating atomic diffusion, which promotes particle coalescence and recrystallization growth.

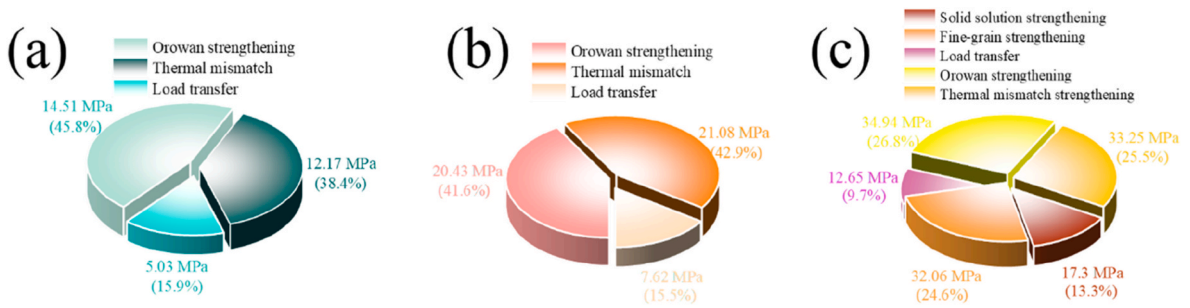

Fig. 11. (a) Contribution values of GNP and Fe_3C in the three strengthening effects. (b) The contribution values of Ti_3SiC_2 and TiC in the three strengthening effects. (c) The contribution values of each of the five strengthening mechanisms in 7Ni composites.

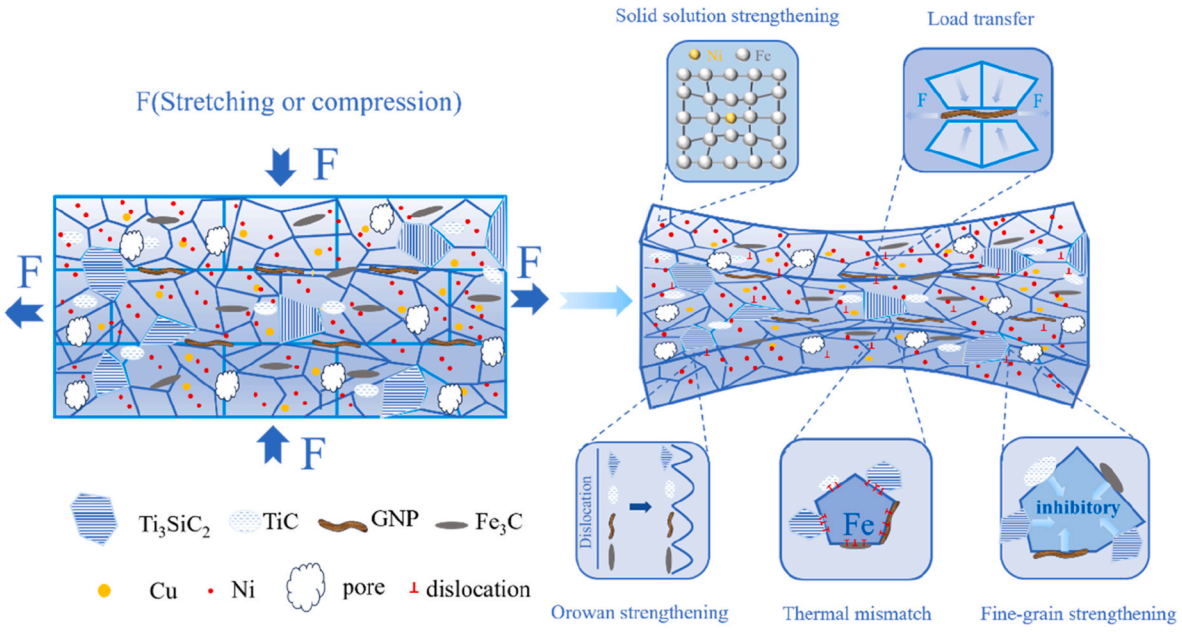

Fig. 12. Schematic diagram of the strengthening mechanism of composite materials.

Data availability statement

The data used to support the findings of this study are available from the corresponding author upon request.

Declaration of competing interest

The authors declare that they have no known competing financial interests or personal relationships that could have appeared to influence the work reported in this paper.

Acknowledgments

This work was supported by Key Laboratory of Infrared Imaging Materials and Detectors, Shanghai Institute of Technical Physics, Chinese Academy of Sciences (No. IIMDKFJJ-21-10). We would like to thank Analytical and Testing Center of Southwest Jiaotong University for partial testing.

References

[1] Zou L, Chen F, Wang H, et al. Influence of porosity on mechanical behavior of porous Cu fabricated via de-alloying of Cu–Fe alloy. Met Mater Int 2019;25(1):83–93. https://doi.org/10.1007/s12540-018-0168-6.
[2] Hedayati R, Yavari SA, Zadpoor AA. Fatigue crack propagation in additively manufactured porous biomaterials. Mater Sci Eng C 2017;76:457–63. https://doi.org/10.1016/j.msec.2017.03.091.
[3] Ritchie RO, Gilbert CJ, Mcnaney JM. Mechanics and mechanisms of fatigue damage and crack growth in advanced materials. Int J Solid Struct 2000;37(1–2):311–29. https://doi.org/10.1016/S0020-7683(99)00096-7.
[4] Gou JF, Lu PP, Wang Y, et al. Effect of nano-additives on microstructure, mechanical properties and wear behaviour of Fe-Cr-B hardfacing alloy. Appl Surf Sci 2016;360:849–57. https://doi.org/10.1016/j.apsusc.2015.11.076.
[5] Nitta H, Miura K, Iijima Y. Self-diffusion in iron-based Fe-Mo alloys. Acta Mater 2006;54(10):2833–47. https://doi.org/10.1016/j.actamat.2006.02.020.
[6] Liu PF, Wu H, Liang LX, et al. Microstructure, mechanical properties and corrosion behavior of additively-manufactured Fe-Mn alloys. Mater Sci Eng A Struct Mater Prop Microstruct Process 2022;852. https://doi.org/10.1016/j.msea.2022.143585.
[7] Bonny G, Domain C, Castin N, et al. The impact of alloying elements on the precipitation stability and kinetics in iron based alloys: an atomistic study. Comput Mater Sci 2019;161:309–20. https://doi.org/10.1016/j.commatsci.2019.02.007.
[8] Gu DD, Shen YF, Lu ZJ. Microstructural characteristics and formation mechanism of direct laser-sintered Cu-based alloys reinforced with Ni particles. Mater Des 2009;30(6):2099–107. https://doi.org/10.1016/j.matdes.2008.08.036.
[9] Zhang J, Jia R, Tan KB, et al. A review of MAX series materials: from diversity, synthesis, prediction, properties oriented to functions. Nano-Micro Lett 2025;17(1):173. https://doi.org/10.1007/s11661-020-05635-1.
[10] Liu B, Sun J, Zhao J, et al. Hybrid graphene and carbon nanotube–reinforced composites: polymer, metal, and ceramic matrices. Adv Compos Hybrid Mater 2024;8(1):1. https://doi.org/10.1007/s42114-024-01074-3.
[11] Yang Y, Song X, Li XJ, et al. Recent progress in biomimetic additive manufacturing technology: from materials to functional structures. Adv Mater 2018;30(36). https://doi.org/10.1002/adma.201706539.
[12] Gao Y, He J, Jiang J, et al. Homogenizing interfacial shear stress in brick-and-mortar structured composites via gradient modulus for enhanced mechanical properties. Acta Mech Sin 2024;40(6):424091. https://doi.org/10.1007/s10409-024-24091-x.
[13] Deng A, Shu R, Sun H, et al. Microstructure and mechanical properties of graphene reinforced porous Fe-7.5Cu composites fabricated by microwave sintering. Powder Technol 2025;464:121273. https://doi.org/10.1016/j.powtec.2025.121273.
[14] Lei QA, Xiao Z, Hu WP, et al. Phase transformation behaviors and properties of a high strength Cu-Ni-Si alloy. Mater Sci Eng A Struct Mater Prop Microstruct Process 2017;697:37–47. https://doi.org/10.1016/j.msea.2017.05.001.
[15] Xu QZ, Ai X, Zhao J, et al. Comparison of Ti(C,N)-based cermets processed by hot-pressing sintering and conventional pressureless sintering. J Alloys Compd 2017;710. https://doi.org/10.1016/j.jallcom.2014.08.261. 880-880.
[16] Hebda M, Debecka H, Miernik K, et al. Spark plasma sintering of low alloy steel modified with silicon carbide. Arch Metall Mater 2016;61(2):503–8. https://doi.org/10.1016/j.ceramint.2012.05.003.
[17] Tekoglu E, O'brien AD, Bae JS, et al. Metal matrix composite with superior ductility at 800 °C: 3D printed In718+ZrB_2 by laser powder bed fusion. Compos B Eng 2024;268. https://doi.org/10.1016/j.compositesb.2023.111052.
[18] Xu J, Zhang J, Bao L, et al. Preparation and bioactive surface modification of the microwave sintered porous Ti-15Mo alloys for biomedical application. Sci China Mater 2018;61(4):545–56. https://doi.org/10.1007/s40843-017-9098-2.
[19] Matli PR, Fareeha U, Shakoor RA, et al. A comparative study of structural and mechanical properties of Al-Cu composites prepared by vacuum and microwave sintering techniques. J Mater Res Technol 2018;7(2):165–72. https://doi.org/10.1016/j.jmrt.2017.10.003.
[20] Agrawal D. 12 - microwave sintering of metal powders. In: Chang I, Zhao Y, editors. Advances in powder metallurgy. Woodhead Publishing; 2013. p. 361–79. https://doi.org/10.1533/9780857098900.3.361.
[21] Roy R, Agrawal D, Cheng J, et al. Full sintering of powdered-metal bodies in a microwave field. Nature 1999;399(6737):668–70. https://doi.org/10.1038/21390.
[22] Golewski GL. Using digital image correlation to evaluate fracture toughness and crack propagation in the mode I testing of concretes involving fly ash and synthetic nano-SiO_2. Mater Res Expresss 2024;11(9). https://doi.org/10.1088/2053-1591/ad755e.
[23] Golewski GL. Investigating the effect of using three pozzolans (including the nanoadditive) in combination on the formation and development of cracks in concretes using non-contact measurement method. Advances In Nano Research 2024;16(3):217–29. https://doi.org/10.12989/anr.2024.16.3.217.
[24] Xi XY, Zheng YX, Zhuo JB, et al. Mechanical properties and hydration mechanism of nano-silica modified alkali-activated thermally activated recycled cement. J Build Eng 2024;98. https://doi.org/10.1016/j.jobe.2024.110998.

[25] Xi XY, Zheng YX, Zhuo JB, et al. Influence of water glass modulus and alkali content on the properties of alkali-activated thermally activated recycled cement. Constr Build Mater 2024;452. https://doi.org/10.1016/j.conbuildmat.2024.138867.
[26] Golewski GL, Xi X, Zheng Y, et al. Experimental evaluation of Mode II fracture and microstructure of matrix-aggregate bond of concrete with crushed limestone. Case Stud Constr Mater 2025;23:e05183. https://doi.org/10.1016/j.cscm.2025.e05183.
[27] Li DX, Jiang XS, Sun HL, et al. Influence of copper-coated graphene films on mechanical and damping properties of bionic laminar CuAlMn matrix composites. J Mater Res Technol 2024;33:2153–63. https://doi.org/10.1016/j.jmrt.2024.09.222.
[28] Yang JS, Ye F, Cheng LF, et al. Phase evolution and reaction mechanism during synthesis of Ti_3SiC_2 from Ti-Si-C and Ti-SiC-C systems. J Alloys Compd 2023:962. https://doi.org/10.1016/j.jallcom.2023.171018.
[29] Wang MX, Zhu H, Yang GJ, et al. Solid-solution strengthening effects in binary Ni-based alloys evaluated by high-throughput calculations. Mater Des 2021;198. https://doi.org/10.1016/j.matdes.2020.109359.
[30] Abu-Oqail A, Samir A, Essa ARS, et al. Effect of GNPs coated Ag on microstructure and mechanical properties of Cu-Fe dual-matrix nanocomposite. J Alloys Compd 2019;781:64–74. https://doi.org/10.1016/j.jallcom.2018.12.042.
[31] Felege GN, Gurao NP, Upadhyaya A. Microstructure, microtexture and grain boundary character evolution in microwave sintered copper. Mater Char 2019;157. https://doi.org/10.1016/j.matchar.2019.109921.
[32] Zuo C, Xu L, Sun Y, et al. Effect of interface bonding and properties of graphite/copper composites by microwave pressure sintering. J Alloys Compd 2024;976:173009. https://doi.org/10.1016/j.jallcom.2023.173009.
[33] Magnus C, Cooper D, Ma L, et al. Microstructures and intrinsic lubricity of in situ Ti_3SiC_2–$TiSi_2$–TiC MAX phase composite fabricated by reactive spark plasma sintering (SPS). Wear 2020;448–449:203169. https://doi.org/10.1016/j.wear.2019.203169.
[34] Zuo CH, Xu L, Sun YF, et al. Effect of interface bonding and properties of graphite/copper composites by microwave pressure sintering. J Alloys Compd 2024;976. https://doi.org/10.1016/j.jallcom.2023.173009.
[35] Yu VB, Rybakov KI, Semenov VE. High-temperature microwave processing of materials. J Phys Appl Phys 2001;34(13):R55. https://doi.org/10.1088/0022-3727/34/13/201.
[36] Ping D-H, Chen H, Xiang H. Formation of θ-Fe_3C cementite via θ′-Fe_3C (ω-Fe_3C) in Fe–C alloys. Cryst Growth Des 2021;21(3):1683–8. https://doi.org/10.1021/acs.cgd.0c01533.
[37] Younes A. Effects of nickel content and annealing temperature on the magnetic characteristics of nanostructured FeCu alloys. J Mater Sci Mater Electron 2024;35(7):535. https://doi.org/10.1007/s10854-024-12291-3.
[38] Capek J, Vojtech D. Effect of sintering conditions on the microstructural and mechanical characteristics of porous magnesium materials prepared by powder metallurgy. Mater Sci Eng C 2014;35:21–8. https://doi.org/10.1016/j.msec.2013.10.014.
[39] Zhang T, Liu W, Yin Z, et al. Effects of the addition of Cu and Ni on the corrosion behavior of weathering steels in corrosive industrial environments. J Mater Eng Perform 2020;29(4):2531–41. https://doi.org/10.1007/s11665-020-04738-5.
[40] Zhao M, Xiong DB, Tan ZQ, et al. Lateral size effect of graphene on mechanical properties of aluminum matrix nanolaminated composites. Scr Mater 2017;139:44–8. https://doi.org/10.1016/j.scriptamat.2017.06.018.
[41] Li GT, Yu TY, Zhang N, et al. The effect of Ni content on phase transformation behavior of NiTi alloys: an atomistic modeling study. Comput Mater Sci 2022;215. https://doi.org/10.1016/j.commatsci.2022.111804.
[42] Huang XL, Wu GH, Zhang Q, et al. Compressive properties of open-cell Fe-Ni foams. Mater Sci Eng A Struct Mater Prop Microstruct Process 2008;497(1–2):231–4. https://doi.org/10.1016/j.msea.2008.07.032.
[43] Susilowati SE, Fudholi A, Sumardiyanto D. Mechanical and microstructural characteristics of Cu-Sn-Zn/Gr metal matrix composites processed by powder metallurgy for bearing materials. Results Eng 2022;14. https://doi.org/10.1016/j.rineng.2022.100377.
[44] Tavakoli A, Liu R, Wu XJ. Improved mechanical and tribological properties of tin-bronze journal bearing materials with newly developed tribaloy alloy additive. Mater Sci Eng A Struct Mater Prop Microstruct Process 2008;489(1–2):389–402. https://doi.org/10.1016/j.msea.2007.12.030.
[45] Deng A, Shu R, Sun H, et al. Microstructure and mechanical properties of graphene reinforced porous Fe-7.5Cu composites fabricated by microwave sintering. Powder Technol 2025;464:121273. https://doi.org/10.1016/j.powtec.2025.121273.
[46] Zhou C, Ye QB, Zhao T, et al. Strengthening and toughening mechanisms in Ni-alloyed steel: enhancing the integral stability of retained austenite. Mater Sci Eng A Struct Mater Prop Microstruct Process 2022;852. https://doi.org/10.1016/j.msea.2022.143703.
[47] García-Macías E, Guzmán CF, Saavedra Flores EI, et al. Multiscale modeling of the elastic moduli of CNT-reinforced polymers and fitting of efficiency parameters for the use of the extended rule-of-mixtures. Compos B Eng 2019;159:114–31. https://doi.org/10.1016/j.compositesb.2018.09.057.
[48] Rupert TJ, Trenkle JC, Schuh CA. Enhanced solid solution effects on the strength of nanocrystalline alloys. Acta Mater 2011;59(4):1619–31. https://doi.org/10.1016/j.actamat.2010.11.026.
[49] Zhang D. Ultrafine grained metals and metal matrix nanocomposites fabricated by powder processing and thermomechanical powder consolidation. Prog Mater Sci 2021;119:100796. https://doi.org/10.1016/j.pmatsci.2021.100796.
[50] Montazeri A, Panahi B. MD-based estimates of enhanced load transfer in graphene/metal nanocomposites through Ni coating. Appl Surf Sci 2018;457:1072–80. https://doi.org/10.1016/j.apsusc.2018.07.038.
[51] Bai C, Tu J, Yang L, et al. Synergistic enhancement of strength-ductility through multi-phase heterogeneous structure induced by SiC particle addition in CoCrFeNi high entropy alloy. Mater Sci Eng, A 2025;924:147753. https://doi.org/10.1016/j.msea.2024.147753.
[52] Shan H, Li Y, Wang S, et al. Friction stir processing of wire arc additively manufactured Al-Zn-Mg-Cu alloy reinforced with high-entropy alloy particles: microstructure and mechanical properties. J Alloys Compd 2025;1020:179476. https://doi.org/10.1016/j.jallcom.2025.179476.
[53] Jin K, Gao YF, Bei H. Intrinsic properties and strengthening mechanism of monocrystalline Ni-containing ternary concentrated solid solutions. Mater Sci Eng A Struct Mater Prop Microstruct Process 2017;695:74–9. https://doi.org/10.1016/j.msea.2017.04.003.
[54] Roy A, Sreeramagiri P, Babuska T, et al. Lattice distortion as an estimator of solid solution strengthening in high-entropy alloys. Mater Char 2021;172. https://doi.org/10.1016/j.matchar.2021.110877.